

**High resolution study of local stress inside
alumina - Micro Mechanical Analysis Using Laser
Scanning Confocal Microscope**

Dissertation

zur Erlangung des Grades

„Doktor der Naturwissenschaften“

am Fachbereich Chemie, Pharmazie und Geowissenschaften
der Johannes Gutenberg-Universität Mainz

Yun Chen

geb. in Wuxi, P. R. China

Mainz 2007

Dekan: Uni.-Prof . Dr. P. Langguth

Erster Berichterstatter: Prof. Dr. H.-J. Butt

Zwiter Berichterstatter: Prof. Dr. T. Basche

Tag der mündlichen Prüfung: den 18. Dezember 2007

Die vorliegende Arbeit wurde in der Zeit von October 2005 bis September 2007
am Max-Planck-Institut für Polymerforschung
unter der Betreuung von Herrn Prof. Dr. H.-J. Butt angefertigt.

Contents:

Abstract.....	3
Symbols and abbreviations	5
1. Introduction.....	7
1.1 Mechanical contact.....	7
1.2 Theoretical aspects for stress analysis.....	8
1.2.1 Analytical formulation	8
1.2.2 Numerical simulation.....	12
1.3 Experimental stress analysis.....	13
1.3.1 Strength test	13
1.3.2 Photoelasticity photography.....	15
1.3.3 Fatigue tests by impact and micro indentation	17
1.3.4 Fluorescence and Raman spectroscopy	18
1.4 Ruby – stress sensitive material	19
1.4.1 General properties.....	19
1.4.2 Pressure gauge for hydrostatic environment.....	21
1.4.3 Spectral shift under non-hydrostatic environment.....	21
1.4.4 Brittleness and ductility	22
1.5 Laser scanning confocal microscopy	23
1.6 One vs. two-photon excitation.....	25
2. Materials and methods	27
2.1 Materials.....	27
2.2 Instruments	28
2.3 Setup.....	29
2.4 Numerical simulations by FEM	30
2.5 Experimental procedures.....	31
2.6 Data analysis - determination of conversion factor.....	33
3. Results and discussion	36
3.1 Calculation of stress by simulations	36

3.2 Defocusing effect and refractive index matching.....	39
3.3 Ruby fluorescence spectra and spectral shift under stress	45
3.4 General stress distribution within the ruby sphere	47
3.5 Stress distribution at the microcontact	52
3.6 Quasi-static compression and stress development	57
3.7 Two-photon excitation.....	63
3.8 Repeated loading cycles	67
3.9 Periodic loading using piezo vibration.....	77
4. Summary and conclusion.....	86
Bibliography	89
Acknowledgement	98
Curriculum Vitae.....	100

Abstract

The aim of this work is to measure stress in a micro sphere of hard materials subjected to uniaxial loads applied by two rigid plates and to compare it to theoretical predictions. I described to my knowledge the first direct measurement of stress at a mechanical microcontact. To measure the internal stress distribution, I compressed ruby spheres ($\alpha\text{-Al}_2\text{O}_3\text{:Cr}^{3+}$, 150 μm diameter) between two sapphire ($\alpha\text{-Al}_2\text{O}_3$) plates. Ruby shows a fluorescence spectrum when being excited. The fluorescence spectrum peaks at 694.3 nm (R_1 line) and 692.8 nm (R_2 line). It played the role of a stress sensor. The peaks shift to longer wavelengths under compression and the distance of shift can be related to stress by a proper conversion coefficient. Since the ruby sphere is transparent and polished to optical level, fluorescence spectra can be obtained from inside the sphere. Thus a laser scanning confocal microscope was used to excite fluorescence at any positions inside the ruby sphere with spatial resolution of about $1\times 1\times 1\ \mu\text{m}^3$. Figure 1 shows the scheme of the experimental setup.

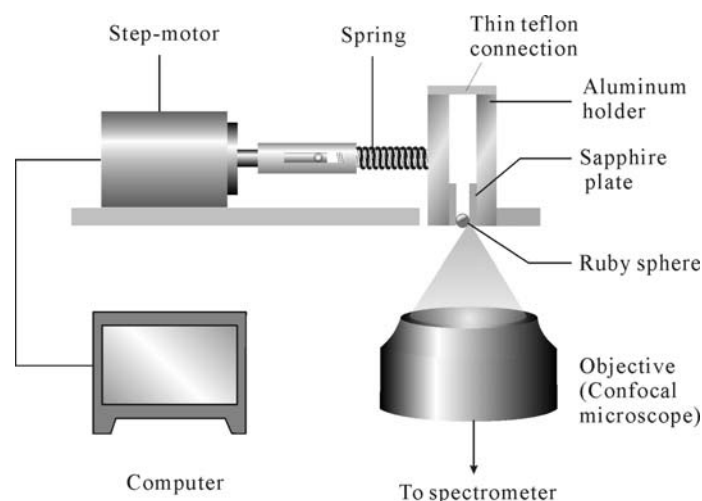


Fig. 1. Schematic sketch of the experimental setup.

Under static external loading forces, the stress distribution within the center plane of the ruby sphere was measured directly for the first time and compared to Hertz's law. The measurement was in good agreement with theoretical prediction as well as the FEM simulations. The stress across the contact area showed a hemispherical profile. The measured contact radius was in accord with the value

calculated by Hertz's equation.

By stepwise increasing of load, stress-vs-force curves were obtained and used to analyze the stress development at the contact region. The results showed spike-like decrease of stress after entering non-elastic phase. This was attributed to the formation and coalescence of microcracks, which led to relaxing of stress. In the vicinity of the contact area luminescence spectra with multiple peaks were observed. This indicates the presence of regions of different stress, which are mechanically decoupled.

Repeated loading cycles were used to study the fatigue of ruby at the contact region. Progressive fatigue was observed when the load exceeded the lower limit of the critical load. As long as the load did not exceed the critical load of yield stress-vs-load curves were still continuous and could be described by Hertz's law with a reduced Young's modulus. Once the load exceeded the critical load, spike-like decreases of the stress could be observed.

Vibration loading with higher frequencies was applied by a piezo. Redistributions of intensity on the fluorescence spectra were observed and it was attributed to the repopulation of the domains of different elasticity within the optical detecting volume. Two stages of behavior under vibration loading were observed. In the first stage continuous damage carried on until certain limit, by which the second stage, e.g. breakage, followed in a discontinuous manner.

Symbols and abbreviations

σ_1	principal stress along the loading axis
σ_2	principal stress in radial direction
σ_3	principal stress in tangential direction
σ	total stress (sum of three principal stresses)
R_1	ruby fluorescence emission line at 694.2 nm
R_2	ruby fluorescence emission line at 692.8 nm
$\Delta\lambda$	wavelength shift
$\Delta\lambda_0$	maximum wavelength shift within the contact area
E	Young's modulus
E^*	effective Young's modulus
D	damage
ν	Poisson's ratio
a_c	radius of the contact circle
R	radius of the ruby sphere
F	load
F_c	critical load
P	vertical pressure within the contact area
P_0	maximum of the vertical pressure
P_Y	critical contact loading pressure at the first yield
P_C	critical contact loading pressure of tensile fracture
Y	yield stress
H	hardness
DSP	model of stress distribution in a sphere by Dean, Sneddon and Parsons
HO	model of stress distribution in a sphere by Hiramatsu and Oka
FEM	finite element method
DEM	discrete element method

DAC diamond anvil cell
LSCM laser scanning confocal microscopy
TPLSC two-photon laser scanning microscopy

Chapter 1. Introduction

1.1 Mechanical contact

Contact mechanics is the study of the deformation of solids that touch each other at one or more points. It is one of the most common interactions between solid objects. The physical and mechanical formulation of this subject is built upon mechanics of materials and theory of elasticity. The applications of contact mechanics also have impacts to our daily life, e.g. in architecture, machine designing, chemical engineering, automobile industry, and recently in microelectromechanical systems (MEMs) and biomechanics, etc.

There are two distinct types of a mechanical contact: “conforming contact” and “non-conforming contact”. A conforming contact is the one in which two bodies touch at multiple points before any deformation takes place (i.e. they “fit” each other). In a non-conforming contact, the shapes of the bodies are dissimilar enough that, under no load, they only touch at a single point. In this case, the contact area is much smaller compared to the size of the objects, and the forces and stresses are usually highly concentrated.

Conforming contact is common in practice if we talk about contact between two flat surfaces at relatively large scales. When scaling down to microscopic dimensions, however, one usually find these contacts consist of numerous microcontacts since most surfaces are normally rough at nano- or microscales (Fig. 1-1). These are by nature non-conforming contacts.

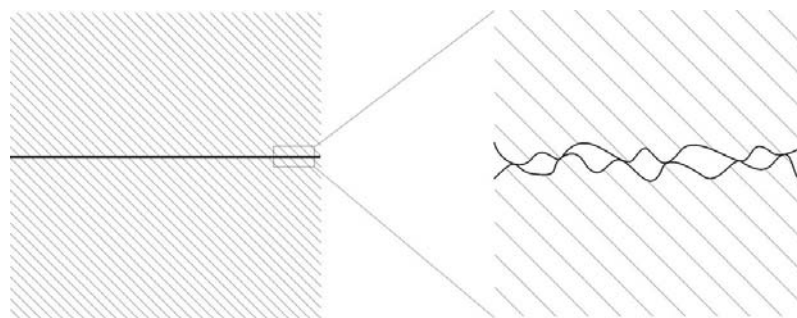


Fig. 1-1. Contact between two flat solid surfaces actually consist of numerous non-conforming contacts at protrusions (roughness) of nano- or microlevel.

Contacts at these microscale asperities (protrusions) are usually much smaller than the apparent contacting area. The pressure is thus much higher than if one calculates the pressure with the apparent contact area. The local stress distributions within these micro bodies are closely related to macroscopic behaviors of the objects, for example, deformation and indentation, friction and attrition, fracture and failure, and so on. Therefore, study of contact mechanics at microscales is important.

A typical model that is used to describe the microcontact is the contact between two spheres or between a sphere and a plate. A lot of theoretical work has been done to describe the stress field inside the sphere, especially the stress distributions at the contact region. The following section will introduce some of the important theories, e.g. Hertz/Huber's prediction, DSP and HO model, etc.

1.2 Theoretical aspects for stress analysis

1.2.1 Analytical formulation

The theory developed by Heinrich Hertz over a century ago remains the foundation for most contact problems encountered in engineering. The original work dates back to the publication of the paper "On the contact of elastic solids" by Hertz in 1882 [1]. In this paper, Hertz formulated the analytical solution for internal stress distributions in an infinite half-plane beneath the contact area of a load applied by an elastic sphere on the surface, giving an onset to the study of modern contact mechanics. It applies to normal contact between two elastic solids that are smooth and can be

described locally with orthogonal radii of curvature. Further, the size of the actual contact area must be small compared to the dimensions of each body and to the radii of curvature. Hertz made the assumption that the contact area is elliptical in shape for such three-dimensional bodies. The equations simplify when the contact area is circular such as with spheres in contact. Though Hertz gave the equations for the stresses inside the half-plane beneath the sphere, he didn't calculate stress distributions within the sphere itself.

For study of stress within a sphere, a model is usually experimentally established as a sphere subjected to uniaxially compressive load between two plates (Fig. 1-2). Such a case is geometrically a simple model that practically illustrates principles of natural processes, e.g. crushing of a rock, etc.

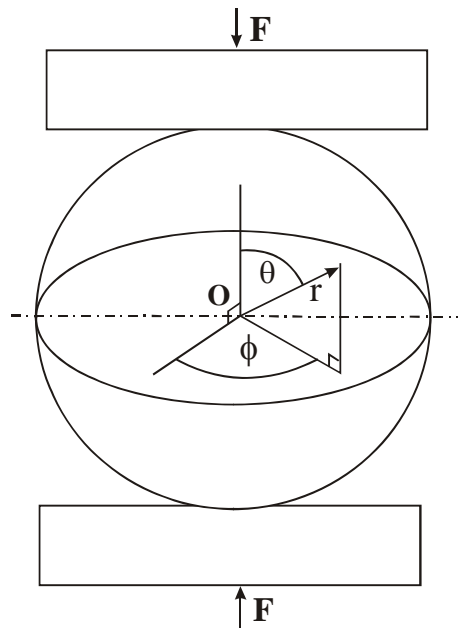


Fig. 1-2. Schematic sketch of a sphere pressed uniaxially between two rigid plates.

It has been well known there are three types of principal stresses in the main stress field in the inner body of a sphere under such conditions: the compressive stress σ_1 , which goes mainly along the loading axis; the radial stress σ_2 , which is perpendicular to σ_1 and in the plane including the loading axis; and the hoop stress σ_3 that is orthogonal to both σ_1 and σ_2 (Fig. 1-3).

The principal stress σ_1 is always compressive within the whole sphere. The principal stresses σ_2 and σ_3 are tensile in the main body, however, are compressive in the contact region.

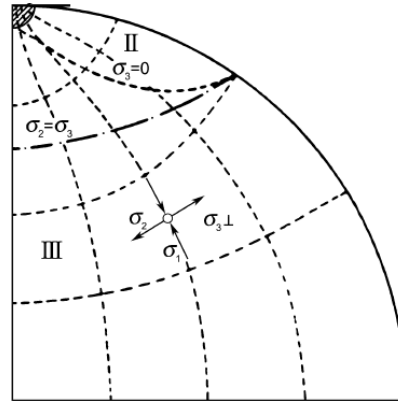


Fig. 1-3. Three principal stresses in a quadrant of the spherical cross-section. σ_1 and σ_2 are in the paper plane; σ_3 is perpendicular to the paper plane [2].

The detailed stress conditions in the contact region are shown in Fig. 1-4, corresponding to the small shadowed area at the top of Fig. 1-3. In this plot, the positive sign is used for tension and the negative sign is used for compression. There are three regions. In region I, all three principal stresses are compressive. In region II, the principal stresses σ_1 and σ_3 are compressive and radial stress σ_2 is tensile. Region III is the main stress field, where σ_1 remains compressive while the radial stress σ_2 and the hoop stress σ_3 are both tensile. Several theories have been developed and they were aimed to determine the directions and magnitude of stress components in any location within the stress field. However, there is no single theory that can describe precisely both the main stress field and the field of contact region.

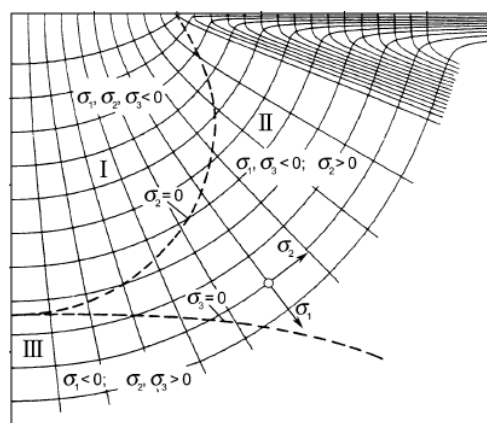


Fig. 1-4. Principal stress trajectories of in the contact region according to Hertz/Huber theory [2].

Dean, Sneddon and Parsons (1952) [3] provided an analysis (referred to as DSP model) on the stress distribution in a decelerating elastic sphere, in which the solution consisted of an infinite series. Hiramatsu and Oka (1966) [4] gave their results (referred to as HO model) in studying the inner stresses of an elastic sphere, which was subjected to the diametrical compression of a pair of concentrated loads. The analytical solutions they developed were similarly in the form of infinite series.

Apart from these two pieces of important work, Lurje (1963) [5] independently developed his model, treating the problem of a sphere lying on a flat surface. Different from Hertz's analysis, he mainly focused on the stress distributions within the sphere rather than under the surface of the plane.

Recently, Shipway and Hutchings made use of the DSP model to treat the problem of uniaxial compression of a sphere [6]. They superimposed two sets of solutions (stress values at θ and $180^\circ - \theta$, symmetrical to the equatorial plane, Fig 1-2), and compared the result with that obtained from the HO model. They found that this treatment had almost of the same validity and had shown the advantage of much greater computational efficiency and simplicity. The curves of maximum tensile stress along the loading axis (Fig. 1-5) indicates that the DSP and HO models numerically agree fairly well [7]. The tensile stress σ_ϕ here is equivalent to the hoop stress σ_3 .

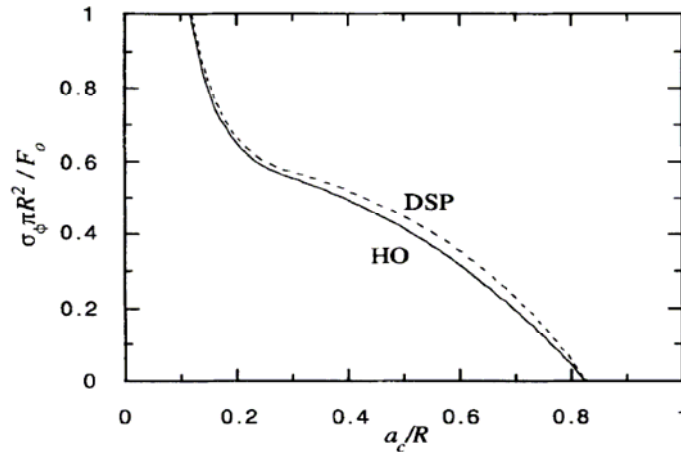


Fig. 1-5. Variation of the maximum tensile stress on the axis with a_c/R for a sphere in uniaxial compression from the extended solutions of DSP and HO model [7].

Based on their work, Gundepudi *et al.* [8] tried to treat more complicated problems of multiaxial loads of a spherical object, which is much closer to the real conditions in most natural processes. They made use of symmetric elements and superimposed stresses obtained from the original DSP model. Chau *et al.* [9] provided another stress analysis for static compression of elastic spheres between two rigid plates by incorporating the Hertz contact theory into the HO model. They compared the failure of a sphere under static compression and impact. Although the maximum contact force at failure was always larger in static compression, a higher energy requirement for the fragmentation in the impact was observed in their study. Hu *et al.* [10] gave an index of tensile strength of brittle particles. In their study the particle was split along an axial plane in different loading conditions. The index of strength reflected the influence of Poisson's ratio and that of the contact area.

1.2.2 Numerical simulation

Analytical descriptions of the stress distribution are complicated, even for simplest geometries. In a practical sense, simulations, such as the finite element method (FEM) or discrete element method (DEM), are efficient tools and have been widely used. By means of FEM the response of an object under developing stresses, i.e.

deformation of the shape, propagations of cracks, initial breakage and final failure, can be captured with high precision.

Simulations also allow efficient investigation of different loading conditions. Stresses along any arbitrary directions could be extracted and the different responses between homogeneous and heterogeneous materials can be compared with each other. Not only simple shaped specimen can be analyzed, but also irregular shaped objects as well.

In simulations, stresses analysis can usually be visualized in forms of fringe contours (a set of iso-stress curves). Apart from displaying a vivid stress field, simulations provide much more information simultaneously, such as displacement, strain and stress, energy release such as acoustic emission, etc [11, 12]. In simulations, it is possible to separate different types of stresses (principal stresses and shear stresses) at a given point.

1.3 Experimental stress analysis

1.3.1 Strength test

A class of uniaxial compression tests that involve the loading to failure of a specimen has been used for determination of compressive and tensile strengths of materials. According to symmetry there are cylinder axial load, sphere compression, and square prism crushing. Strength tests include indentation on a thin plate, cube split, cylinder split and beam split, etc [13]. This method is usually based upon the breakage of the specimen. The case of a spherical body under compression was first tested by Sternberg *et al.* [14]. It was later investigated theoretically by Hiramatsu *et al.* [15], letting the contact width tend to zero, namely, the concentrated load.

Different loading conditions have been studied. During the experiment, the specimen is either shot against a rigid stopper, or it is compressed between two hard pressing medium with different loading speed, dynamically (impact) or statically (compression). The quasi-static crushing of the sphere between two flat plates has

long been used to estimate the tensile strength of brittle spheres [16-18]. Different materials have been tested, for example, glass, metals, ceramics, quartz sand and rocks [19-24].

Upon compression, the material either falls into pieces, or undergoes plastic deformation. In most cases both plastic deformations and cracks occur to the specimen. The analysis is carried out on the maximum loads at which the specimen fails and the shape, size and number of resulting pieces. Because the method is destructive, there is no chance to repeat the experiment a second time with the same specimen. Therefore, many tests must be done to get statistics; otherwise it would be impossible to evaluate properties of the specimen or to estimate the experimental error. The limitation is that it can only be used to estimate maximum tensile strength on the loading axis and generally lack of high accuracy. For example, it was suggested that during quasi-static compression, the maximum tensile stress required for failure is ~ 0.7 times the applied loads divided by the equatorial area of the sphere: $\sigma_f \approx 0.7 \cdot F / \pi R^2$, as given by Hiramatsu and Oka [15], however, argued for a factor of ~ 0.4 by Shipway and Hutchings [6]. Because of complicated loading conditions, the values of the tensile strength can show deviations up to 50%.

Concerning the breakage of spheres by uniaxial compression, an “orange slice” cracking pattern (Fig. 1-6) that cracks are radiated from the loading axis is usually observed [25-27].

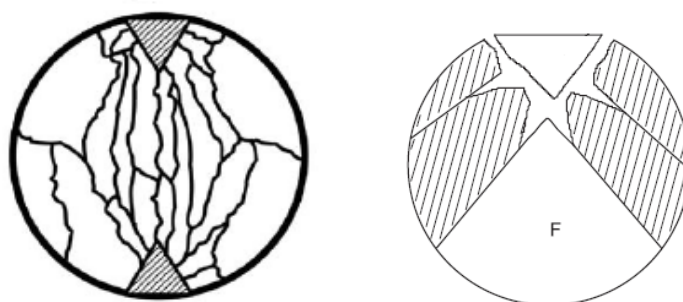


Fig. 1-6. Schematic sketches of the crack pattern in a compressed sphere (left) and an impacted (right) sphere [25, 27].

The propagation of cracks and the number of fragments are significantly

influenced by the size of the sphere and speed of loading. In quasi-static compression or at low impact velocity, there are fewer fragments resulted and the sizes of these fragments are relatively large. For high-speed impact, the number of fragments increased and the so-called “crush zone” formed leading to smashed pieces of material. For smaller sized specimen such effect is attenuated. The crack patterns to some extent show the influence of the internal stresses on the material under loading, but there is still a lack of simple models to interpret the mechanism, and different models are often not valid for both main stress field as well as the contact region.

Due to the development of camera and sensor technologies, it is possible to trace the entire process of loading by slow motion videos [25, 28]. By attaching force transducer to the impactor, the energy release during the loading can also be recorded [29]. This enables obtaining information about the propagation of cracks and visualization of different loading conditions, however, direct measuring of internal stresses is still hardly achieved and the destructive character is inherent. Further more, for small (micro range) objects, the resolution of the camera is not sufficient enough to capture high quality graphs. The crack process lasts so short about $1\sim 10^2 \mu\text{s}$, the response of sensor becomes relatively poor. Therefore, real-time measurement for stress analysis in a micro object under uniaxial compression has hardly been reported up to date.

1.3.2 Photoelasticity photography

Photoelasticity is a method to visualize stress distribution inside a material. Photoelastic materials (e.g. epoxy resin) enable direct observation of the stress patterns in a flat specimen. The advantage of this method is that it can be applied to any arbitrarily shaped objects where mathematical solution becomes cumbersome and is suitable for various loading conditions. The common setup of a photoelasticity experiment is shown in Fig. 1-8. A photoelastic specimen is placed between a polarizer and an analyzer. Loads are applied on the specimen and the fringe patterns representing the internal stress are observed. Information of isochromatics and

isoclinics can be obtained and these fringe patterns enable determination of direction of the principal stress [30]. Isochromatic fringes are contours of constant principal stress difference, i.e. the maximum shear stress and isoclinics are locus along which the principal stresses are in the same direction [31, 32]. The periodicity of the interference stripes indicates the stress gradient in that regime. Some typical fringe patterns in a stressed photoelastic material are shown in Fig. 1-8.

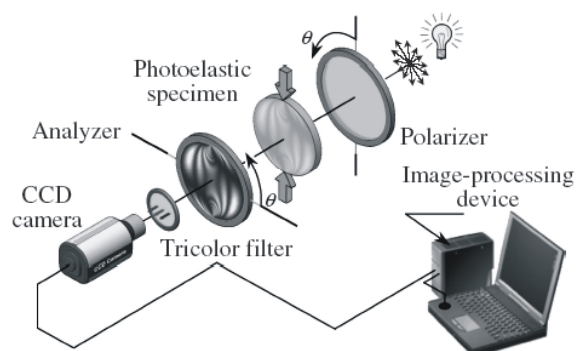


Fig. 1-7. The schematic sketch of experimental setup of photoelasticity imaging [30].

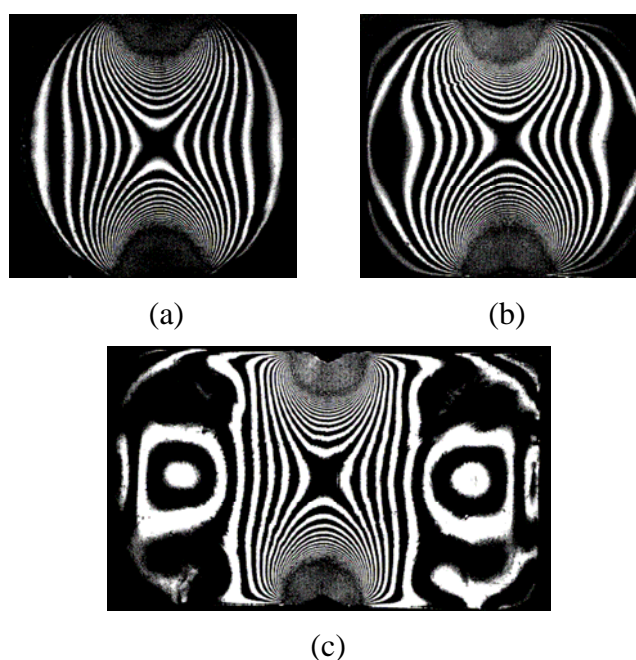


Fig. 1-8. Fringe patterns indicating stress distribution in (a) a disc, (b) a square, and (c) a rectangular specimen of photoelastic material (epoxy resin). Concentrated loading force is applied from top and bottom [4].

Though it is a major experimental method used for analyzing stress distribution within stressed specimens and can be done with great ease, it is not

quantitative in measuring the magnitudes of stress components and is also hard to be applied to 3-dimensional bodies or objects of small length scales.

1.3.3 Fatigue tests by impact and micro indentation

Fatigue tests describe the cyclic failure behavior of materials. There are basically two types of way to conduct fatigue tests: repeated impact and cyclic loading. From the fracture mechanics of materials it is known that the cyclic impact/loading of metallic as well as non-metallic materials leads to the breakage at stresses, which are substantially lower than the failure stress during the static loading. The reduction of fracture strength occurs because of formation and progression of shear zones and microcracks during each cycle [33].

Krogh [34] demonstrated that anorthosite particles become progressively weaker after repetitive impact. Later Pauw [35] confirmed that even when subjected to low-energy impact far below failure stress, particles would eventually break, although many impacts per particle were required. Vervoorn [36] also reported experiments on repetitive ballistic impact of sintered alumina cylinders. Tavares [37] described a decreasing elastic-plastic stiffness of particles during repeated impact and explained the breakage behavior with the formation and progression of damages (Fig. 1-9).

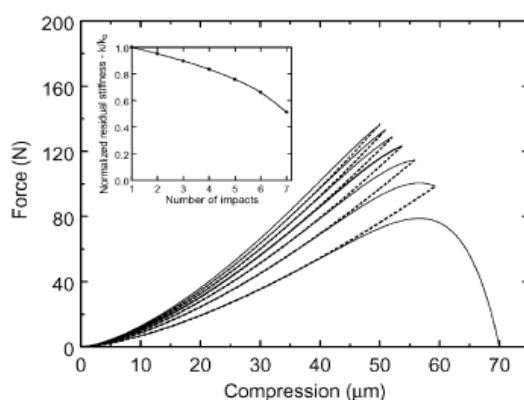


Fig. 1-9. A force-displacement plot in a repetitive impact experiment, in which the curves level down after each impact. The inset shows decreasing of material stiffness [37].

Cyclic loading is more often used to test smaller sized objects by micro indentations. Fatigue under cyclic indentation measurements have been applied using Vickers indenter [38-41], soft metallic cone indenter [42, 43] and spherical wolfram carbide indenter [44-49]. For characterization, surface optical microscopy is usually used to capture the impression after cyclic loading procedures (Fig. 1-10). Two types of damage have been identified, the development and subcritical growth of cone cracks in the tensile stress field near the indentation and the development of a quasi-ductile zone in the compressive area below the indenter. This quasi-ductile zone consists of a network of microcracks.

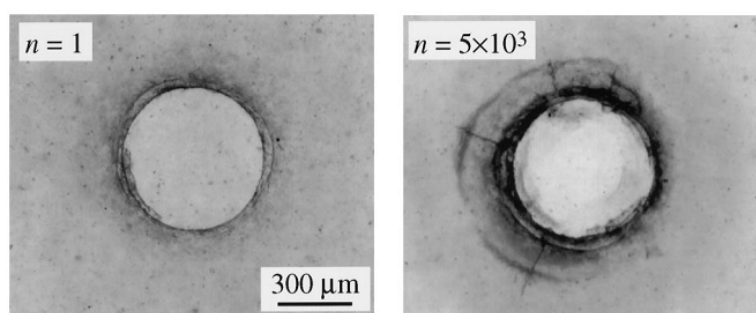


Fig.1-10. Optical micrograph of a Hertzian indentation site, comparing damage after single-cycle and multi-cycle loading [47].

1.3.4 Fluorescence and Raman spectroscopy

The methods introduced above are precluded from investigation across microscopic object due to their relatively low resolutions and surface bound characters. For interests of the stresses at local volumes down to micro range inside the bulk of a specimen, optical spectroscopy is taken into account.

The basis of optical measurement of stresses is piezospectroscopic phenomena. An applied stress strains the lattice of a crystalline material and alters the energy transitions between electronic or vibrational states. In this way, systematic shifts in the wavelengths of fluorescence (Raman) lines can be correlated with external stresses.

Using piezospectroscopic phenomena, stresses within bulk of a transparent object, especially, in crystals can be measured. Equipped with optical facilities,

objects suitable for studying are down to several micrometers level.

Grabner [50] measured the residual stress in a sintered ceramic containing ruby by changes in line frequency and line width. Molis and Clarke [51] studied stresses around indentations in a chromium-doped sapphire with Raman spectroscopy as an optical microprobe. Emerets *et al.* [52] measured the pressure distribution between a spherical diamond indenter and a tungsten carbide plate with a layer of ruby powder sandwiched. Yang and Young [53] used fluorescence spectroscopy to study the deformational micromechanics of α -alumina/glass composites. Zhao *et al.* [54] studied sapphire fibers in polymer matrix by fluorescence spectroscopy and photoelastic method. Hayazawa *et al.* [55] used surface enhanced Raman spectroscopy to study Si-Si bond with a thin layer of Si (30 nm) on top of SiGe composites. Cronin *et al.* [56] detected strain in single-walled carbon nanotubes by resonant Raman spectroscopy. Jiang and Tsukruk [57] also used resonant Raman spectroscopy to measure membrane of carbon nanotubes.

The studies mentioned above mainly focused on macroscopic objects or a small volume beneath the indenter. The stress condition inside the indenter itself has rarely been seen experimentally documented. My work is to explore a bit into this issue. In order to fulfill reasonable detection depth and high spatial resolution, I chose fluorescent ruby microsphere as the stress sensor in combination with laser scanning confocal microscopy.

1.4 Ruby – stress sensitive material

1.4.1 General properties

As a material with piezospectroscopic frequency shift, ruby (Fig 1-11) is a good candidate for its chemical inertance, low thermo expansion coefficient, and good linearity of stress induced frequency shift. Known as a red gemstone, ruby has the chemical composition of α -Al₂O₃: Cr³⁺ and has a hexagonal rhombohedral crystalline structure. The color of ruby varies from light pink (as in my case) to

blood red, which is caused mainly by the doped chromium ions.



Fig. 1-11. Ruby crystals: raw material and polished ones

(<http://www.diamondvues.com/archives/>).

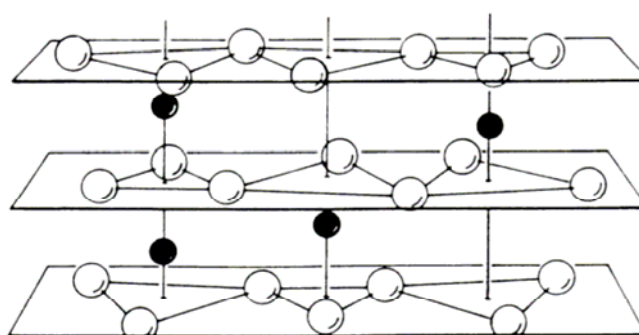


Fig. 1-12. A portion of the lattice of aluminium oxide in which the Al^{3+} ions (dark Circles) are shown between layers of O^{2-} ions (open circles). The optical axis or c axis of the crystal is perpendicular to the planes of oxygen ions. The a axes of the crystal are the lines in the planes connecting the oxygen ions. In ruby, Cr^{3+} ions have taken the place of some of the Al^{3+} . (Picture from Henderson & Imbusch, *Optical Spectroscopy of Inorganic Solids*, 1989, Oxford Science Publications.)

Pure ruby crystal, the chromium doped alpha-alumina (Cr^{3+} : $\alpha\text{-Al}_2\text{O}_3$, Fig. 1-12), shows fluorescence when excited by a source usually providing blue-green light or higher energy. But it can also be excited at near infrared of 782 nm or longer wavelengths via two-photon excitation processes, reported by Wang *et al.* recently [58]. Here, as the photon energy of the NIR laser is lower than that of the fluorescence, it would need simultaneous absorption of two photons to excite the R lines of ruby [59]. Ruby luminescence spectrum has two strong emission lines, R_1

and R_2 , are at 694.3 and 692.8 nm under ambient conditions, respectively. They are due to the ${}^2E \rightarrow {}^4A_2$ transitions of Cr^{3+} .

1.4.2 Pressure gauge for hydrostatic environment

Since 1970s ruby single crystals have been used for pressure calibration in the diamond anvil cell (DAC) measurements as shown in Fig. 1-13 [60]. The diamond anvil cell came to its complete form as a gasketed device with a ruby fluorescence scale inside following the work by J.D. Barnett, S. Block and G.J. Piermarini [61, 62]. It has been designed to create ultrahigh hydrostatic pressure within small volume of confined fluid. Under the hydrostatic compression, both R_1 and R_2 fluorescence emission lines of ruby have the same amount of pressure dependent red shift, about 3.65 \AA/GPa (0.274 GPa/\AA) [63]. Also the ratio of the amplitudes of R_1 and R_2 lines has been observed independent of the pressure, as well as the width of the emission lines at relatively low pressure [64]. The stress induced shift of the ruby fluorescence lines has been observed to be linear to at least 20 GPa with a resolution better than 20~30 MPa [65]. A recent paper by Eggert *et al.* [66] has discussed the calibration at higher pressures (in excess of 100 GPa).

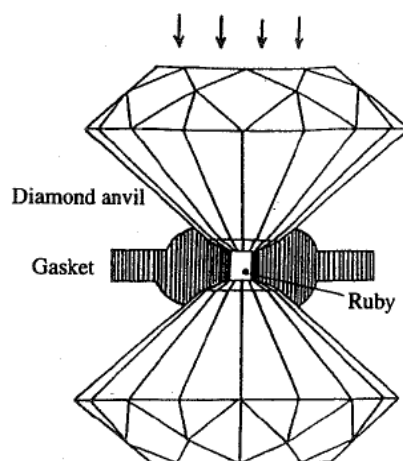


Fig. 1-13: The principle of a diamond anvil cell (DAC) [60].

1.4.3 Spectral shift under non-hydrostatic environment

Under non-hydrostatic conditions (Fig. 1-14), the relations between line

shifts and stresses become more complicated. Different piezospectroscopic coefficient has been obtained when the ruby crystal is compressed along different crystallographic axes, namely, a and c axis. According to the study of Clarke *et al.*, the piezospectroscopic tensor for R_1 and R_2 lines are different, which indicates independent relations between the observed spectroscopic shift and the stress state in the crystal [67-70]. However another important finding is that the shear stresses applied along crystallographic axes do not cause a noticeable wavelength shift of ruby fluorescence [67]. This is regarded as an advantage for approximation of stress distribution in a ruby crystal, since the off diagonal tensors can be neglected, which leads to a much simpler mathematical form [71].

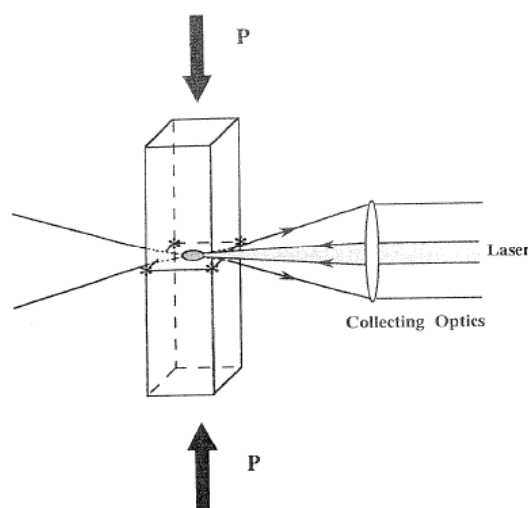


Fig. 1-14. Measuring of wavelength shift of the ruby fluorescence under uniaxial compression (non-hydrostatic) along predetermined crystallographic axis [67].

1.4.4 Brittleness and ductility

Conventionally, alumina (Al_2O_3) is considered as a brittle material. However, when scaling down transition of its mechanical properties occurs. Rhee *et al.* [72] has recently proposed a prediction index, which showed a transition in ceramic materials from brittle fraction to quasi plasticity when the size of the contact radius a_c of a Hertzian contact decreased. Two important parameters, P_Y and P_C were compared. P_Y was the critical contact loading pressure at the first yield and P_C was the critical contact loading pressure of tensile fracture. Both critical loading pressure

values could be determined by experiments. If $P_Y/P_C > 1$, the response was brittle; if $P_Y/P_C < 1$, the response was quasi-plastic, in other word, the material showed certain ductility. For Hertzian contact radius smaller than 1 mm, alumina ($E = 390$ GPa) was quasi-plastic applying criterion of the prediction index P_Y/P_C . Thus, ruby crystal microspheres in my experiments are expected to show non-elastic characteristics. At the microcontact, propagation and coalescence of microcracks dominate the damage and fatigue during loading processes.

1.5 Laser scanning confocal microscopy

To measure local spectral shifts, I used a confocal microscope. The confocal microscopy has its name from the arrangement of the light path. In a confocal microscope, the illumination and detection light paths share a common focal plane, which is achieved by 2 pinholes that are equidistant to the specimen as shown in Fig. 1-15.

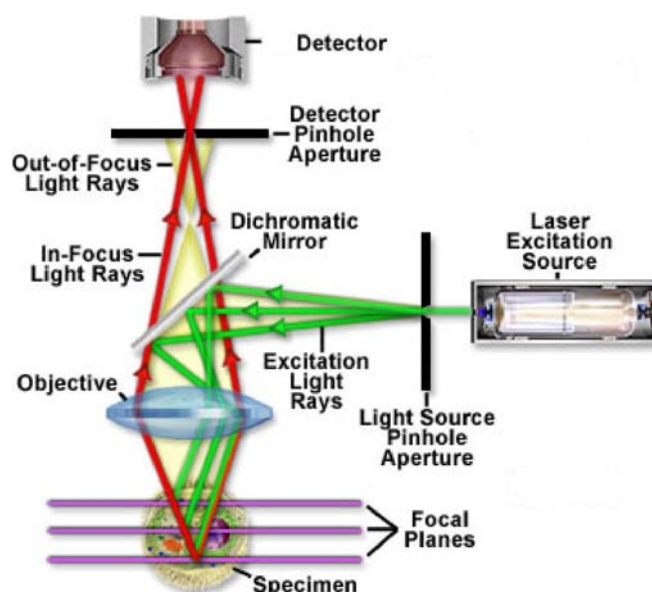


Fig. 1-15: The schematic sketch showing the light paths and in a confocal microscope.

(<http://www.science.uva.nl/>)

Commonly, Krypton/Argon or Helium/Neon mixed gas lasers are used that

can produce a range of different distinct wavelengths. The excitation light rays pass through a light source pinhole and are reflected by a dichromatic mirror to the objective and specimen. The dichromatic mirror is a beam splitter that reflects the wavelengths of the excitation source and is transparent to all other wavelengths. Therefore, the emitted light from the specimen (which normally has a wavelength spectrum above the excitation wavelength) can go through the dichromatic mirror to the detector pinhole and then reach the detector. As a consequence of the pinhole arrangement, light arriving at the detector comes predominantly from a narrow focal plane, which improves the z-resolution significantly compared to conventional microscopy (Fig. 1-16) [73, 74].

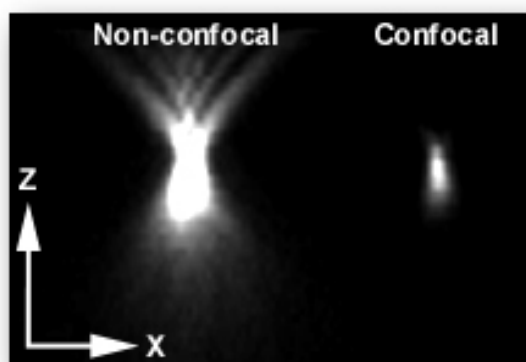


Fig. 1-16: A fluorescent bead (<0.2 microns) imaged non-confocally and confocally, showing the ability of isolating information from individual planes within a specimen.

(www.agheinze.com/)

The elimination of all the out-of-focus light rays enables the achievements in high resolution along axial direction. At the high end, the xy-resolution can be achieved is half of the excitation wavelength, e.g. for the excitation light from a He-Ne laser (543 nm for example) the best lateral resolution is about 270 nm. The z-resolution in axial direction is worse than the xy-resolution. From a practical view, getting a z-resolution just below 1 μm can be expected. With the height discrimination of the confocal microscopy, optical studies of the fractography inside luminescent materials down to sub-micron range have been reported [75].

1.6 One vs. two-photon excitation

In 1931, it was predicted theoretically by Maria Göppert-Mayer [76] that photons of lesser energy together could cause an excitation normally produced by the absorption of a single photon of higher energy in a process called two-photon excitation.

The concept of two-photon excitation is based on the idea that two photons of low energy can excite a fluorophore in a quantum event, resulting in the emission of a fluorescence photon, typically at a higher energy than either of the two excitatory photons. The probability of the near-simultaneous absorption of two photons is extremely low. Therefore a high flux of excitation photons is typically required, usually a femtosecond laser.

If the excited molecule is fluorescent, it can emit a single photon of fluorescence as if it were excited by a single higher energy photon (Fig. 1-17).

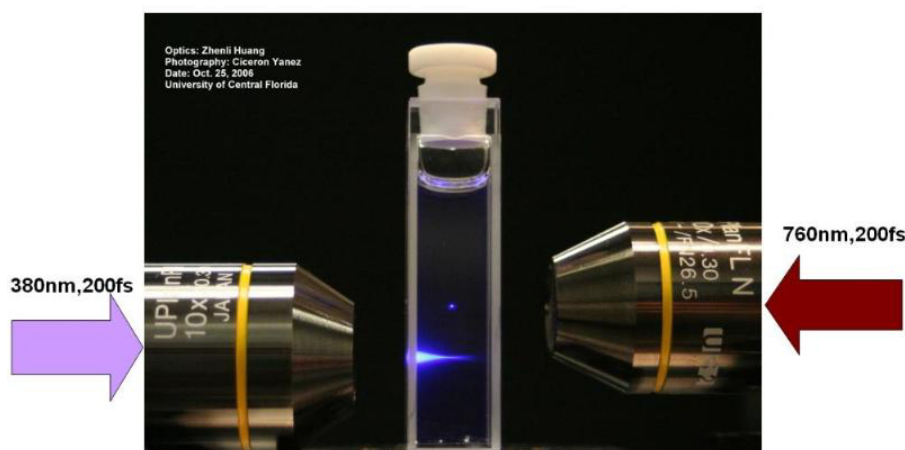


Fig. 1-17. Spatial resolutions of two-photon and one-photon excitation are compared using a diluted solution of fluorophore molecules (<http://belfield.cos.ucf.edu/>).

Two-photon laser scanning microscopy (TPLSM) is a fluorescence imaging technique that allows deeper detection above millimeter range. The TPLSM is a special variant of the multi-photon fluorescence microscopy. It may in some cases be a viable alternative to laser scanning confocal microscopy (LSCM) due to its deeper penetration and reduced phototoxicity [77]. In general, lateral (xy) resolution with

TPLSM is slightly worse than with LSCM using the same fluorophore, because the excitation wavelength is twice as long. The real benefits are in the axial resolution, and in the ability to penetrate more than twice as deep into samples.

Chapter 2. Materials and methods

2.1 Materials

Ruby spheres were purchased from Goodfellow GmbH (Bad Nauheim, Germany). The diameters of the spheres were 150 μm . The composition was: 98.9% Al_2O_3 , 0.9% Cr_2O_3 , and 0.1% Si_2O_3 (weight percentage). Sapphire plates were purchased from Lot-Oriel Group (Germany) with dimensions as 4.7mm \times 4.7mm \times 0.5mm. The plates were optically polished on both sides. Index matching liquids of $n_D^{25} = 1.7$, 1.76, and 1.80 were purchased from Cargille Lab® (Cedar Grove, NJ, USA).

Main characters of the crystalline ruby spheres were verified by X-ray diffraction measurement and compared with the values in literature.

Spheres Parameters	1	2	3	Literature
a (\AA)	4.7640	4.7616	4.8013	4.7591
c (\AA)	13.009	13.009	13.0001	12.9894
V (\AA^3)	255.7	255.3	259.5	254.8

Tab. 2-1. Main parameters of the three measured ruby crystal obtained by X-ray diffraction.

Results obtained with three ruby spheres are shown in Tab. 2-1, in which a and c are parameters of the unit cell of the crystal, and V is the unit cell volume. The

crystal properties agreed with literature quite well, indicating the ruby spheres had the properties of Al₂O₃ single crystal. However, I should need to point out that although the material was verified as single crystal, some local defect or grain boundaries could still be present due to manufacturing process, e.g. milling, etc. Thus heterogeneity to certain extent might exist.

2.2 Instruments

An inverted laser scanning confocal microscope (LSM 510-ConfoCor 2, Carl Zeiss, Germany) was used for exciting and collecting fluorescent light from ruby crystal. The objective used was a Zeiss Plan-Neofluar 40× multi-immersion with the numerical aperture NA = 0.9 and working distance 130 μm.

Both one-photon and two-photon excitations were used to excite ruby fluorescence. For one-photon excitation, the light source was a helium-neon laser of 543 nm in wavelength. The maximum output for the helium-neon laser was 1 mW. For two-photon excitation, a Ti:Sapphire laser (Mai Tai, Spectra Physics, USA) was used. The wavelength was tunable between 780~920 nm and provided 100 fs pulses at 80 MHz repetition rate and average power of approximately 1 W. In this study, the emission wavelength of Ti:Sapphire laser was set to 800 nm that allowed the efficient two-photon excitation of ruby fluorescence. The pinhole for the one-photon excitation was 80 μm and for the two-photon excitation, 500 μm. For both excitations, resolution in xy plane was less than 1 μm. The axial resolution was about 2-4 μm for one-photon excitation and ~ 1 μm for two photon excitation.

A SpectraPro® 2300i system (Acton Research Corporation, Acton, MA, USA), including a monochromator, a spectrograph and a CCD camera, was used to record the fluorescence spectra.

Scanning electron microscopy (SEM) was used to take pictures of the impressions on the ruby sphere after compression. A low-voltage SEM (LEO 1530 Gemini) was used to avoid coating with a conducting layer.

2.3 Setup

The ruby sphere was clamped between a pair of sapphire plates, which were glued to the homemade pressing device (Fig.2-1).

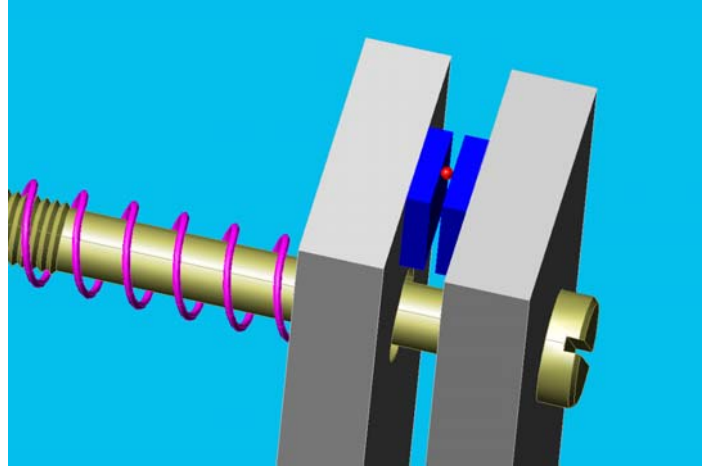


Fig. 2-1. Ruby sphere clamped between two sapphire plates: view from the bottom.

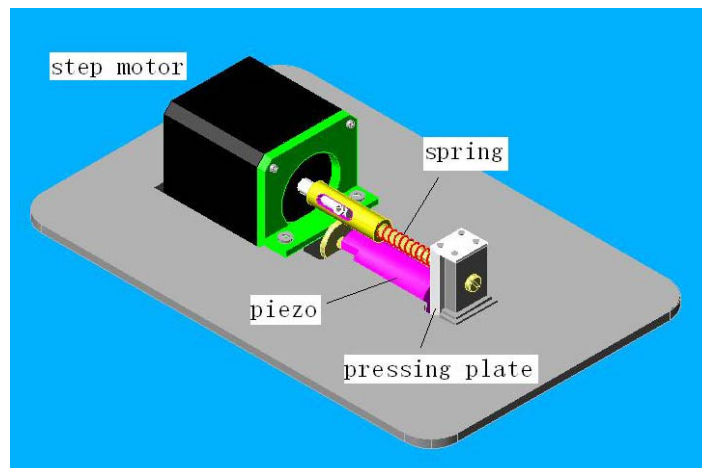


Fig. 2-2. Three-dimensional view of the homemade pressing device.

The functions of main parts of the pressing device (Fig. 2-2) are the followings. The spring connecting step motor and the pressing plate had a spring constant of ~ 5500 N/m. The step motor could compress or expand the spring by ~ 0.0028 N per step. A piezo could be used to vibrate the pressing plate. The piezo was controlled by a closed-loop circuit and the vibration frequency could vary from 10^{-3} ~ 10^3 Hz, with a maximum external load of 1000 N. During vibration, the positional error was

estimated to be less than 50 nm. For stress mapping at constant loads and low speed loading cycles, step motor was used. The piezo was used for higher frequency vibration loading (> 0.1 Hz).

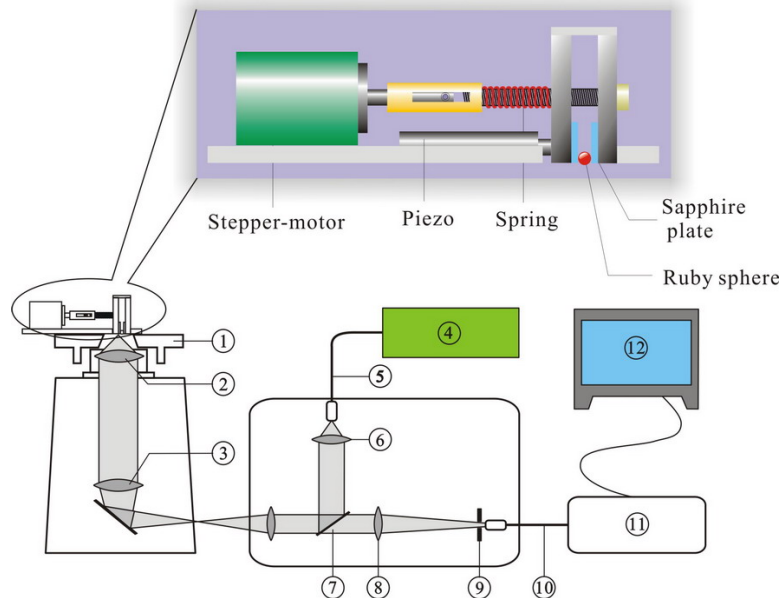


Fig. 2-3. Experimental setup: (1) microscope stage, (2) objective, (3) tube lens, (4) He-Ne (or Ti: Sapphire) laser, (5) single-mode fiber, (6) collimator, (7) beam splitter, (8) pinhole optics, (9) pinhole, (10) optical fiber, (11) spectrometer, and (12) computer.

During the experiment the pressing device was placed on the stage above the objective lens (Fig. 2-3) and the clamped ruby sphere was immersed in the meniscus of an index matching liquid formed in between the stage and the objective lens. The stage with the pressing device on it could move in stepwise. The smallest step length was $1 \mu\text{m}$ and it could be positioned with resolution of $0.25 \mu\text{m}$. The helium-neon (or Ti: Sapphire) laser was used to excite ruby fluorescence. The fluorescent light was guided into the spectrometer, in which the inbuilt spectrograph was exposed for predetermined time. The data was transferred in to the connected computer.

2.4 Numerical simulations by FEM

Thomas Haschke in University of Siegen contributed to the simulation with

FEMLab®. I also evaluated analytical solutions of DSP model and model of Lurje's. Input of expressions and calculation was done with Maple® and plotting with Origin®. It was not successful to get reasonable results from the analytical solutions. FEM simulations were finally chosen to examine our experimental data.

2.5 Experimental procedures

Four types of experiments were conducted, they were

- Stress mapping at a constant load
- Stress recording with increasing load
- Repeated loading cycles
- Periodic loading using piezo vibrating

a. Stress mapping at a constant load

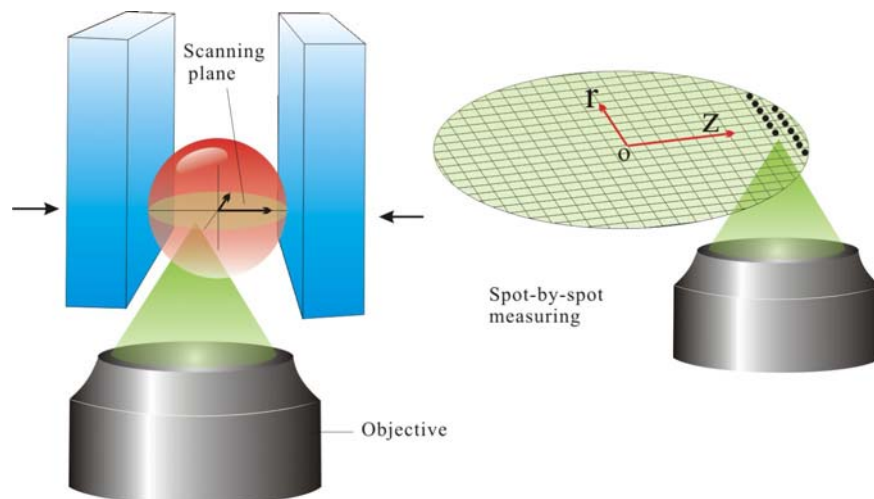


Fig. 2-4. (Left) During the stress mapping, the focus of the exciting laser beam moved on the horizontal center plane inside the ruby sphere, including the loading axis. (Right) The scanning was in a spot-by-spot manner.

In this static stress mapping, the ruby sphere was clamped by a constant predetermined loading force (~ 4 N). A desired plane (normally the horizontal central

plane) in the ruby sphere was scanned (Fig. 2-4 left). The equatorial plane was scanned spot by spot (Fig. 2-4 right). During the measurement, one spectrum was taken at each spot. The exposure time was usually 5 seconds. Then the stage was moved 5 μm to the next spot and the next spectrum was recorded, etc. In total, normally 813 spots covering the whole scanning plane were measured in a single experiment, which lasted 3 hours.

b. Stress recording with increasing load

To observe changes in stress in the microcontact region between the ruby sphere and the sapphire plate, I kept the stage still and the laser beam focused on the contact between the ruby sphere and non-movable sapphire plate. Choosing of this contact point was meant to reduce the relative shift of the laser focus due to deformation of the ruby sphere. The ruby sphere was first mounted with the initial force less than 0.05 N. During the experiment, the stepper motor was used to compress the spring and so to increase the load on the sphere at 0.055 N per step. After each load-increasing step, one spectrum was taken. The external force was increased until the ruby sphere broke or just before its breakage.

c. Repeated loading cycles

In this procedure, the laser focused also on the contact between the ruby sphere and non-movable sapphire plate. The ruby sphere was first mounted with the initial force less than 0.05 N. The loading force was then gradually increased by the step motor, with a step increment of 0.055 N, to a maximal load of 1.1 N. After that it was gradually unloaded to zero again. At each step it took 5 seconds to record a fluorescence spectrum with the spectrometer. Afterwards the load was increased in the same manner to 2.2 N, decreased to zero, increased to 3.3 N... etc. For the last cycle, the maximum load was often off the predetermined values, since in this cycle failure of the contact area occurred and the loading process was usually held until the ultimate decrease of stress. The whole experiment lasted 2-3 hours.

d. Periodic loading using piezo vibrating

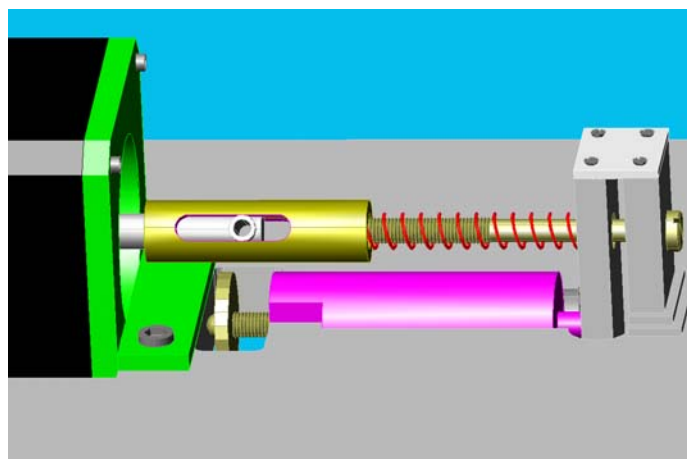


Fig. 2-5. A detailed look of the piezo driving section in the homemade pressing device.

In the vibration loading experiments, the ruby sphere was again first mounted using the step motor. The initial force exerted by the spring was less than 0.05 N. Then the piezo was tuned to approach the compressing plate (Fig. 2-5). An electrometer was used to monitor the voltage from the piezo. When the end of the piezo touched the pressing plate, there is a noticeable fluctuation on the electrometer. Then the piezo was fixed and the initial touching force was estimated to be 0.1-0.5 N. In the experiment, the piezo was kept vibrating at predetermined frequencies and magnitudes. Meanwhile, fluorescence spectra were recorded with an exposure time of 5 seconds each during the vibration. The magnitudes (displacement) of vibration up to 6 μm and the frequencies 0.2, 1, 5, 10, 20, and 200 Hz were used. At each frequency, at least 10 spectra were recorded in order to get an average result.

2.6 Data analysis - determination of conversion factor

The R_1 line shift was determined using a double-peak Lorentz fitting and used for stress calculation. For complicated spectral shapes (multi-peaked), the shift of R_1 line was usually taken directly from the spectra.

To calculate the stress, a mean conversion factor was needed. The principle of relating an observed line shift in a fluorescence spectrum to stress has been previously

described by Grabner [50]. He measured stresses in polycrystalline alumina containing Cr^{3+} . A simplified form was demonstrated by Molis [51] and Ma [68]

$$\Delta\nu = (2\Pi_a + \Pi_c)P$$

in which $\Delta\nu$ was the change of radiation energy, Π_a and Π_c were piezospectroscopic coefficients perpendicular to and along the c (C_3) axis of alumina, respectively, and P was the hydrostatic pressure. In my experiments, however, the ruby sphere was under non-hydrostatic pressure. Following Molis and Ma's treatment, I modified their formulation into $\Delta\lambda = \frac{(2\Pi_a + \Pi_c)}{3}\sigma$, where $\Delta\lambda$ was the wavelength shift of the R_1 lines and the "total stress" σ was defined as sum of three components $\sigma = \sigma_1 + \sigma_2 + \sigma_3$.

Author	$\Pi_c \parallel C_3$ (R_1)	$\Pi_a \perp C_3$ (R_1)
Schawlow [78]	0.084 nm/Gpa	0.15 nm/Gpa
Feher [79]	0.086 nm/Gpa	0.127 nm/Gpa
He [67]	0.74 nm/Gpa	0.146 nm/Gpa
Kaplyanskii [80]	1.4 cm^{-1} /GPa	3.12 cm^{-1} /GPa
Mean	0.078 nm/Gpa	0.143 nm/Gpa

Tab. 2-2. Piezospectroscopic coefficients of R_1 fluorescence line shift parallel and perpendicular to the C_3 axis in a ruby crystal.

Under non-hydrostatic conditions, the wavelength shift of R_1 (also R_2) lines depended on the crystallographic direction. For compression parallel to the C_3 axis, the wavelengths shift was 0.078 nm/GPa (R_1); perpendicular to it the wavelength shift was 0.143 nm/GPa (R_1) (mean values from Refs. [67, 78-80], Tab. 2-2). Therefore an effective mean conversion factor of 0.12 nm/GPa was obtained and could be applied to calculate the total stress σ with a good approximation. Since the results from more than 20 experiments using different spheres showed similar stress values (within error of 10%), I concluded the relative orientation of the ruby crystal had no great influence

on the fluorescence line shift at the contact region. This justified the use of the mean conversion factor.

Chapter 3. Results and discussion

3.1 Calculation of stress by simulations

The simulation was done by FEMLab® in cooperation with Thomas Haschke from University of Siegen. We used the 3D structural mechanics module COMSOL Multiphysics (version 3.3) including the COMSOL Multiphysics post processing routine for interpolation. An unstructured tetrahedron mesh was applied, which was automatically refined one time. The approximate number of elements in the base mesh and the degree of freedom, respectively, were 12,500 and 55,500 without grid adaptations during the solving steps. We used a Young's modulus of $E = 350$ GPa and a Poisson's ratio of $\nu = 0.25$. The load was applied as in the spherical cap model assuming equal mechanical properties of the plate and the sphere material.

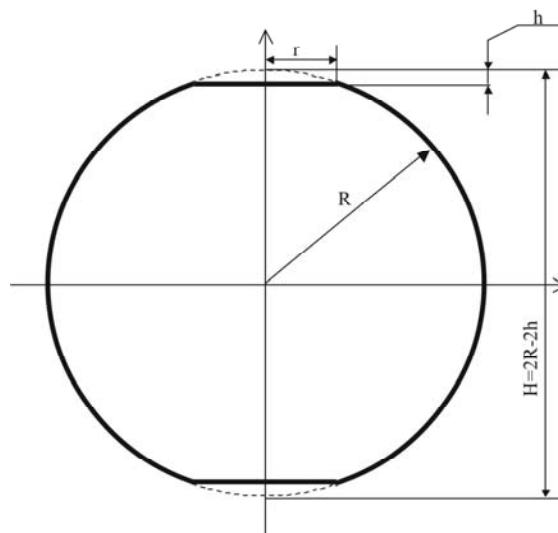


Fig. 3-1. Schematic sketch of the spherical cap model applied to simulation. R is the radius of the ruby sphere; r is the contact radius and h the indentation depth.

A sketch of the spherical cap model for simulation is shown in Fig. 3-1. The radius of the sphere R equaled $78\ \mu\text{m}$. The contact area was examined by scanning electron microscope (SEM) and the contact radius r was measured to be $13\text{-}15\ \mu\text{m}$ at a load of $\sim 4\ \text{N}$. Thus h , the indentation depth, was calculated to be about $1.5\ \mu\text{m}$.

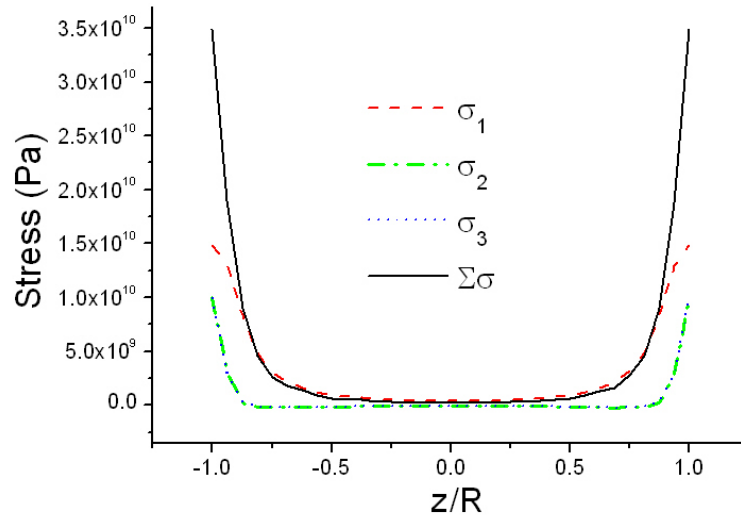


Fig. 3-2. Curves of three principal stresses σ_1 , σ_2 , σ_3 and the total stress $\Sigma\sigma$ along the loading axis. R is the radius of the sphere and z/R represents positions along the axis.

The distribution of the three principal stresses σ_1 , σ_2 , σ_3 , and the total stress $\Sigma\sigma = \sigma_1 + \sigma_2 + \sigma_3$ along the loading axis is shown in Fig. 3-2. The applied load is about $4\ \text{N}$. The compressive σ_1 is always above the other two principal stresses and above zero, which means σ_1 is compressive along the entire axis. Near to the contact region, σ_1 and σ_2 (σ_3) are of close magnitudes, with a difference of about $2/3$. The total stress $\Sigma\sigma$ goes in between σ_1 and σ_2 (σ_3) in the middle of the axis and takes the highest position close to the contact regions. This indicates that σ_2 and σ_3 are tensile in the middle section of the loading axis and near the contact regions they become compressive.

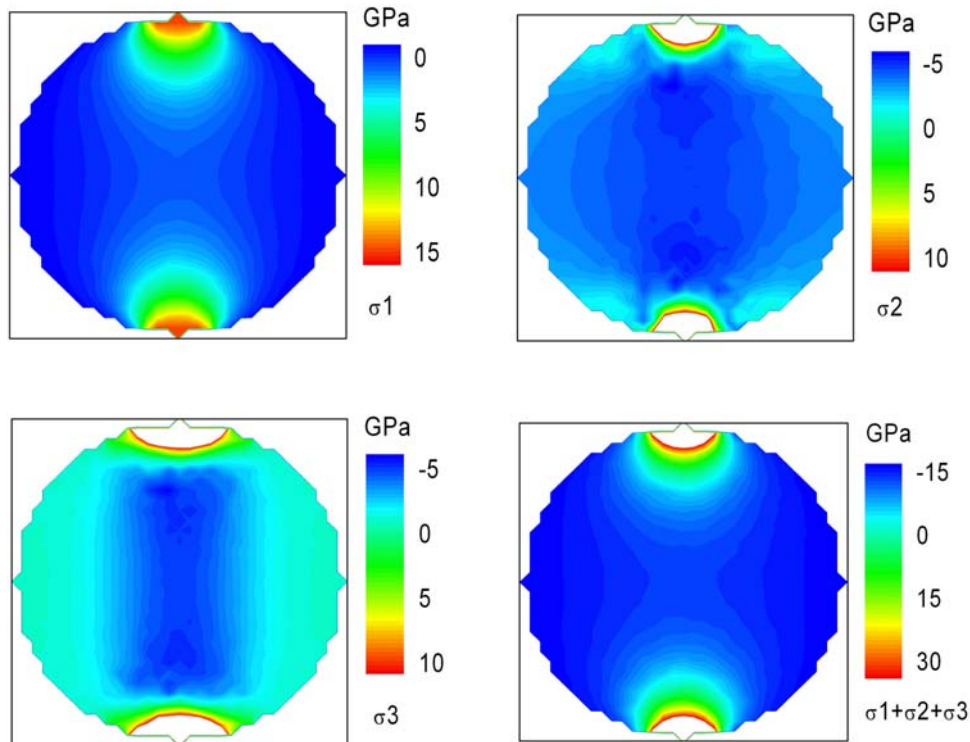


Fig. 3-3. Stress distribution contours of σ_1 , σ_2 , σ_3 and the total stress $\Sigma\sigma$ calculated by simulation program FEMLab® with 3D structural mechanics module COMSOL Multiphysics. External loads are applied from top and bottom.

The 2D stress contours (Fig. 3-3) provide us with a complete view of the stress distribution. The vertical principal stress σ_1 is compressive throughout the whole sphere. The radial stress σ_2 and hoop stress σ_3 are compressive within regions near to the contacts, and then inverted to be tensile towards the inner domains of the sphere, which consists with the theoretical predictions. The total stress also gives a reasonable range of magnitude compared to calculation. Therefore, the spherical cap model by FEM simulations was adopted as the numerical measure for examining my experimental results.

3.2 Defocusing effect and refractive index matching

Ruby sphere used in my experiment as the stress sensor has a high refractive index of about 1.755. Such a high refractive index have to be matched by the surrounding environment, otherwise the excitation laser beam will be refracted at the interface and lose its focus. To find out how much the refraction could affect the final results, I scrutinize the locus of laser beam focus inside the ruby sphere when no index matching is applied.

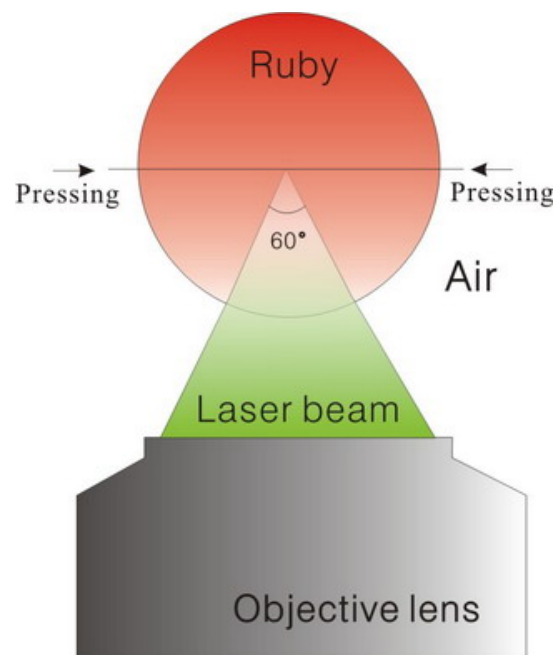


Fig. 3-4: Schematic sketch of the light path of the laser beam when it focuses in the center of the ruby sphere. The size of the sphere is exaggerated for a convenient view.

The horizontal centerline across the sphere (Fig. 3-4) is the line on which I'd like the laser to focus. When the laser focuses in the center of the sphere, all incoming light beams are normal to the ruby-air interface that although refraction happens anyway at the interface, no shift of the focus occurs. When the laser beam moves away from this position, however, focal spot will no longer sit on the horizontal line but shift elsewhere.

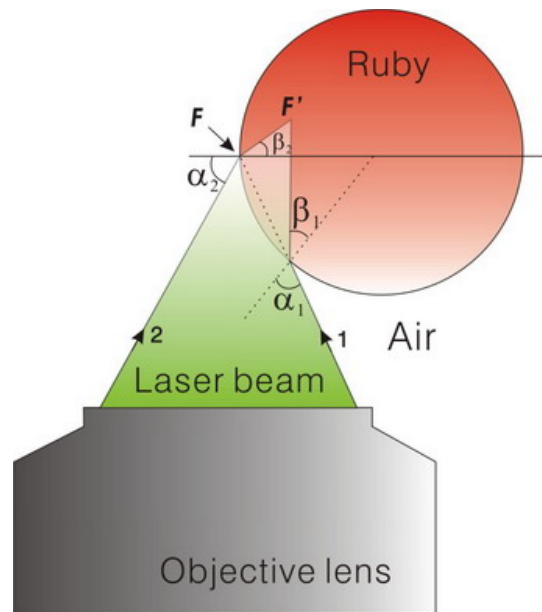


Fig. 3-5: Schematic sketch of the light path of the laser beam when it focuses at the boundary of the ruby sphere.

For simplicity, I examine another extreme case, in which the laser is supposed to focus on the edge of the equatorial plane of the sphere (Fig. 3-5). The point F is the point where the laser should have focused. However, due to refraction the laser beam deviates when it enters the ruby/air interface. I take two rays from the periphery of the light cone as representatives. For ray 1 on the right, the incidence angle α_1 is 60 degrees. According to the equation of refraction $\frac{\sin(\alpha_1)}{\sin(\beta_1)} = 1.76$, the refraction angle β_1 equals 29.5 degrees. The same result can be expected for incidence angle α_2 and refraction angle β_2 . The final position of the laser beam focus inside the sphere shifts from F to F' . Examining into all incident laser rays within the light cone, the incidence angle varies from 60 to 90 degrees. This results in a variation of the refraction angle from 29.5 to 34.6 degrees, which meant that apart from the shifting of laser focus away from the predetermined position, there is also an effect of defocusing. This can lead to an enlarged optical detecting volume and decrease the spatial resolution of the confocal microscope. Thus the matching of refractive index of the ruby and that of the surrounding environment is necessary.

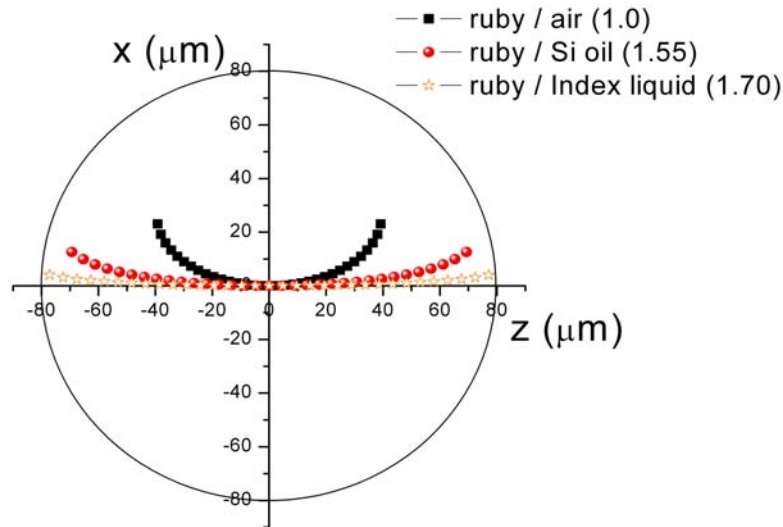


Fig. 3-6. Locus of the laser beam focus inside the ruby sphere with three different ruby/environment interfaces are calculated using the geometry in Fig. 3-5. The predetermined track of the laser focus moves along z -axis. The origin of the coordinate system allocates center of the sphere.

The locus of laser focus inside the ruby sphere is calculated with different environments (Fig. 3-6). The geometry in Fig. 3-5 is used for approximation. The laser focus is supposed to move along the z -axis if it were not refracted. Three ruby/environment interfaces are compared.

In case of ruby/air interface the shift is large. The deviation increases when the beam moves away from the center and the focus shifts above the z -axis. In horizontal direction the focus can hardly exceed half of the full length.

If the sphere is immersed in silicon oil, the shifting of focus is reduced. The locus of the laser focus bends less above z -axis and extends more towards the contact regions.

If an index matching liquid of 1.70 is used, the shift of focus becomes even smaller so that when the laser focuses at the contact point, the focus is shifted by no more than $6 \mu\text{m}$.

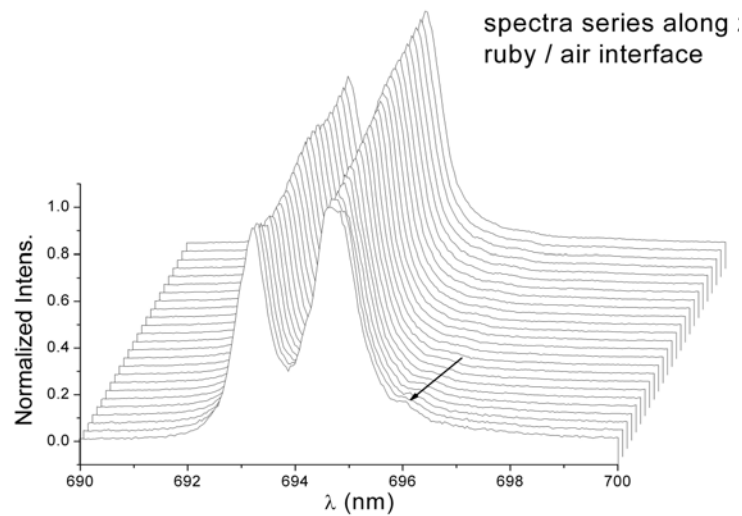


Fig. 3-7. A series of ruby fluorescence spectra were taken along the z-axis when the ruby sphere was observed in the air.

The above calculations are also tested by experiments. Figure 3-7 shows a series of ruby fluorescence spectra that are recorded along the z-axis without index matching. No obvious spectral shift caused by high stresses can be seen on the whole series of spectra. Only on last one at the bottom (indicated by the arrow), there is some tiny peak looming. This implies that the optical detecting volume may have included a little of high stress region, which has almost totally submerged in the strong fluorescence intensity from the low stress region.

The improvement is achieved with index matching using silicon oil (Fig. 3-8). In this case, high stress region can be observed when the laser focuses at the contact regions. Several curves at top and bottom of the series of the fluorescence spectra show peak shifting to the longer wavelength range. Though the distance of shifts is still far below what is expected, the optical detecting volume obviously goes further into the highly stressed region. Nevertheless, it suggests that a more accurate index matching is required.

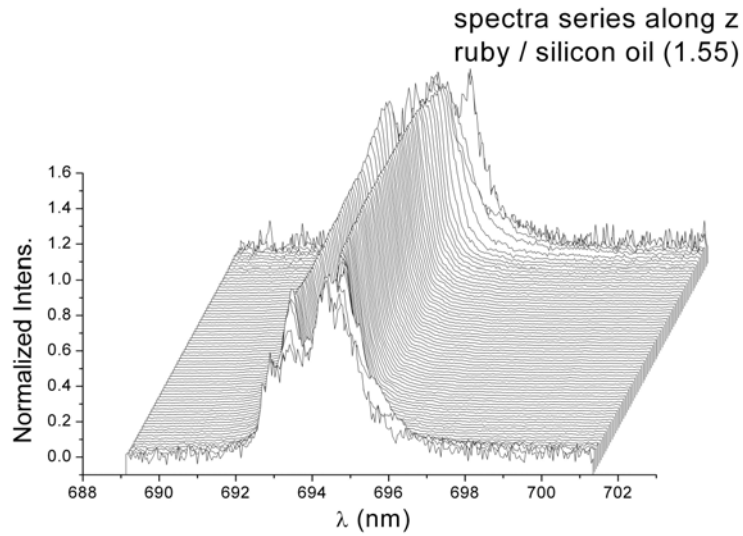


Fig. 3-8. A series of ruby fluorescence spectra were taken along the z-axis when the ruby sphere was immersed in silicon oil with refractive index of 1.55.

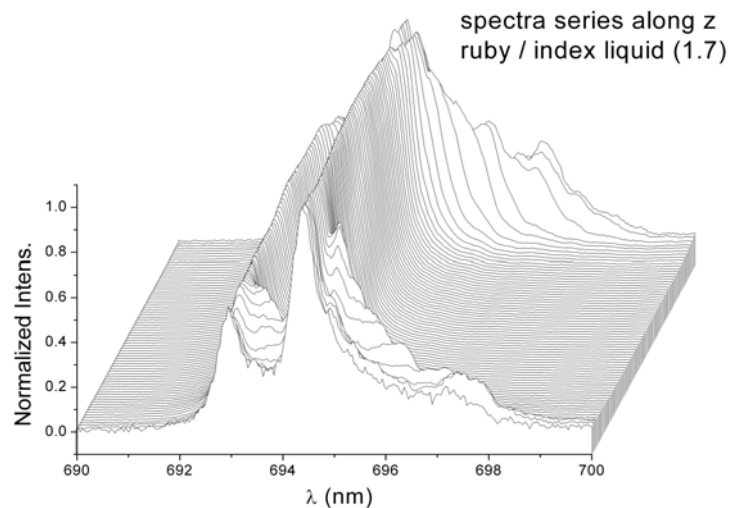


Fig. 3-9. A series of ruby fluorescence spectra were taken along the z-axis when the ruby sphere was immersed in the refractive matching liquid with refractive index of 1.70.

The series of fluorescence spectra recorded in a refractive index matching liquid ($n = 1.7$) are shown in Fig. 3-9. More than a few spectra at top and bottom of the series now show distinct peak shifting. The original peaks are still visible without any sign of shifting and meanwhile maintain rather strong intensity, however, a unique determination of the peak shift is possible. There is still a difference of

indices between the index matching liquid (1.70) and ruby (~ 1.755) so that deflecting and defocusing of laser focus still exist, a problem I can hardly get rid of for this optical system. Using an index matching liquid with even less discrepancy might further decrease the effect of refraction and defocusing and thus enhance the desired signal.

3.3 Ruby fluorescence spectra and spectral shift under stress

A typical spectrum of the ruby fluorescence at zero load shows two peaks at (694.27 ± 0.05) nm and (692.84 ± 0.03) nm at 20°C . The full widths at half maximum are 0.57 nm and 0.48 nm, respectively (Fig. 3-10a). When a compressive stress is applied the emission lines shift to longer wavelengths (Fig. 3-10b).

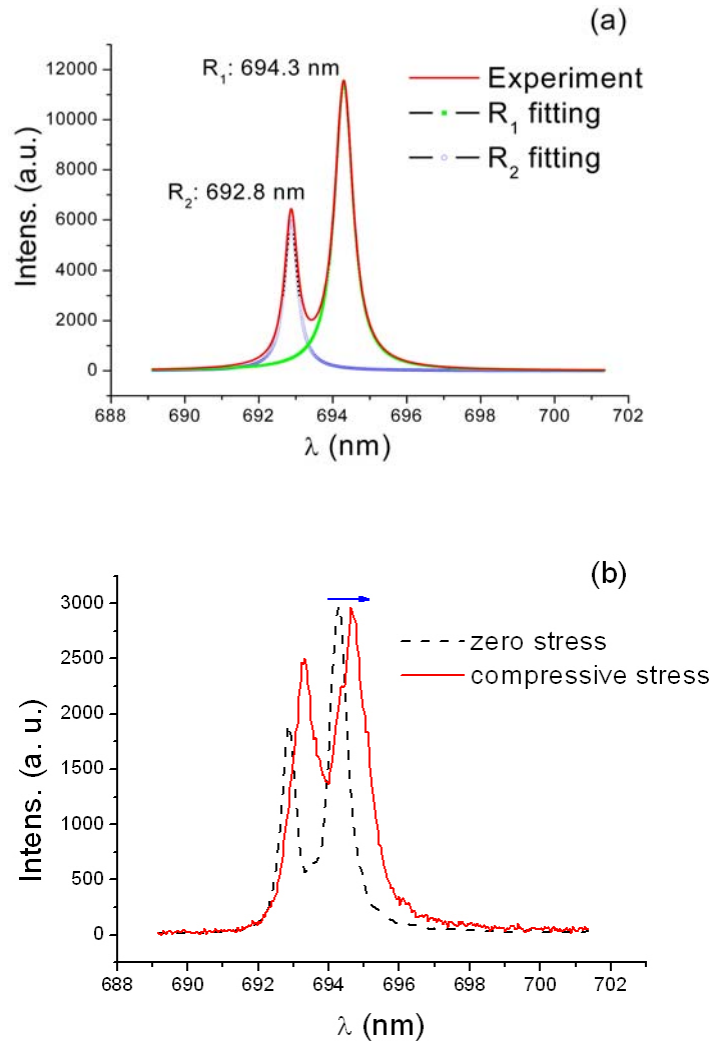


Fig. 3-10. (a) Typical ruby fluorescence spectrum. (b) Peak shift of ruby fluorescence spectrum to longer wavelength when subjected to compressive stress.

In case of very high compressive stress, the typical ruby fluorescence spectrum obtained in my experiment is shown in Fig. 3-11. An index matching liquid of $n = 1.76$ was used for all the spectra shown hereafter unless otherwise mentioned. The

spectrum normally consists of two parts: the shifted part and the unshifted part. For simplicity, I usually take the first peak on the right side as the shifted R_1 peak and use it for calculation, assuming this shift represents the highest local stresses. The unshifted part of the fluorescence spectrum is considered to be the result of multi-scattering. It will be discussed in more details in the forthcoming chapter.

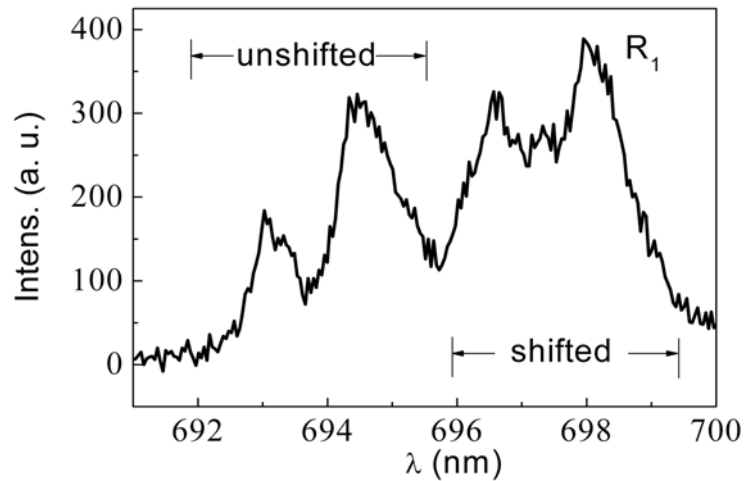


Fig. 3-11. Typical ruby fluorescence spectrum recorded under highly compressive stress.

On the right is the shifted part and on the left is the unshifted part.

3.4 General stress distribution within the ruby sphere

A stress map of experimental result in comparison with simulations at an external loading force of ~ 4 N is shown in Fig. 3-12. The top half represents the experimental result and the bottom half is the result of simulations. The conversion factor 0.12 nm/GPa has been used for calculation of the total stress.

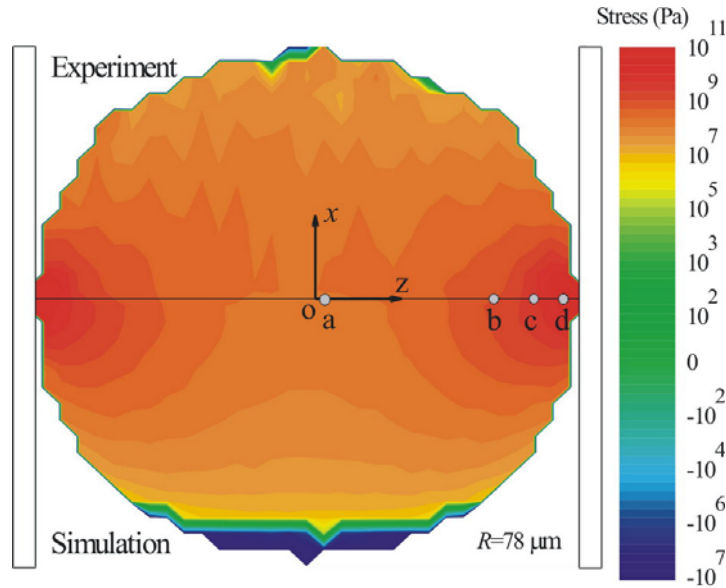


Fig. 3-12. Stress distribution in a ruby sphere compressed between two sapphire plates at a load of ~ 4 N. The He-Ne laser was used for experiment. The top half shows experimental results while the bottom half displays the result of simulations. The minus sign indicates tension and the positive sign for compression.

Stress distribution by measurement is in good agreement to that by simulations (Fig. 3-16) [81]. The compressive stress along the loading axis is maximal at the two contact areas and decreases toward the center of the sphere. In the middle the stress is minimal as it is distributed over a large cross-sectional area. At the equator the stresses σ_2 and σ_3 along the periphery are tensile and dominate the total stress. This small tensile stress is observed as a line shift toward shorter wavelengths. The matching of experiment and simulation is better near the contact region than near to the center part. In the middle the experimental contour shows zigzags. This is because at the contact region, the spectral shift is more obvious and easier to determine while in the middle

of the sphere the spectral shift is sometimes vague to measure.

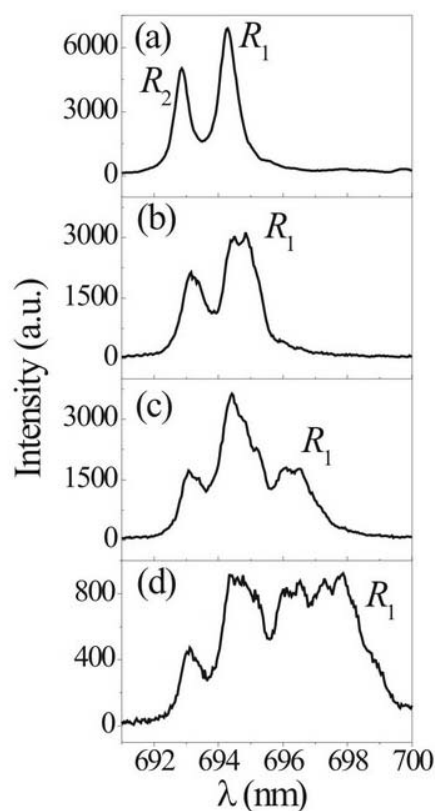


Fig. 3-13. Fluorescence spectra measured along the centerline at positions $z = 0, 63, 75,$ and $77 \mu\text{m}$ indicated by dots 'a' to 'd' in Fig. 3-12, respectively. Index matching liquid $n = 1.76$ was used.

A series of representative fluorescence spectra from different positions along the loading axis are shown in Fig. 3-13. The peaks shift to longer wavelengths in sequence (a) to (d), i.e. from center of the sphere to the contact region. The peak height from (a) to (d) shows a significant decrease. When using the $n = 1.7$ index matching liquid, the total intensity of fluorescence emission may decrease by a factor of ≈ 7 . Change from 1.7 to 1.76 index matching liquid results in decrease of total intensity by a factor of 3-4 (as is the case in Fig. 3-13), which may be a more reasonable value according to the following: when the laser beam moves from center to the contact region, the compressing sapphire plate, according to spatial relations, blocks half of the exciting laser light. Meanwhile, only half of the fluorescence emission can be

collected by the objective (it might be a little more than half because part of the other half of the emitted fluorescence light could also be reflected by the wall of the sapphire plate). This leads to around a four-fold intensity decrease and can account for a large part of the intensity loss. The above observation indicates when using different matching liquids the defocusing of laser focus might have an influence on the intensity distribution of excitation as well as emission of fluorescence.

A noticeable feature of these spectra is that the original fluorescence under zero-stress condition remained unshifted. One reason could be the effect of multi-scattering. This can happen in the bulk of the sphere or between the sphere and the sapphire plates. Fluorescence from space other than the laser focus can by chance get into the objective after being scattered. I had great difficulty in getting rid of the background of the unshifted peaks. However, by changing the index matching liquid, I was able to diminish the background peak intensity dramatically at the contact region without having to influence the shifted peak intensity. The contrast between the spectra taken with index matching liquid of 1.7 to that of 1.8 is shown in Fig. 3-14. The background is largely reduced while the shifted peaks are relatively enhanced. All peak positions are maintained.

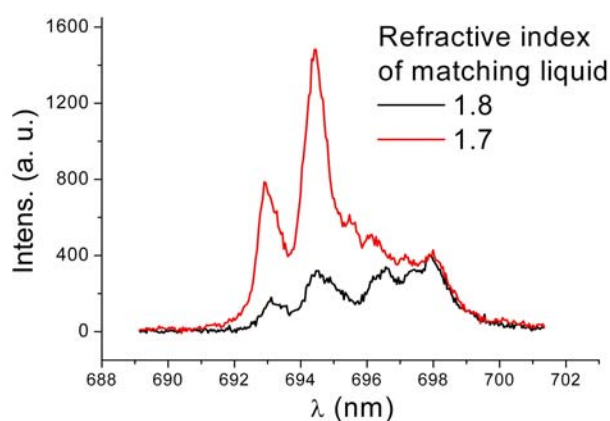


Fig. 3-14. Ruby fluorescence spectra recorded at the contact region under high compression. When refractive index matching liquid of 1.7 was replaced for that of 1.8, the background was significantly reduced.

However, a perfect index matching over the whole load range is impossible

because with increasing load the refractive index of ruby at the contact region changes. The order of magnitude of this effect can be estimated by estimating the increase in density from $\sigma/3E \approx \Delta\rho/\rho$. Here, ρ is the density of ruby and $\Delta\rho$ is the increase in density. The factor three was added to convert the total stress as defined above to an “equivalent” hydrostatic pressure. With a maximum of $\sigma = 30$ GPa in the contact region the density increase during loading is 3%.

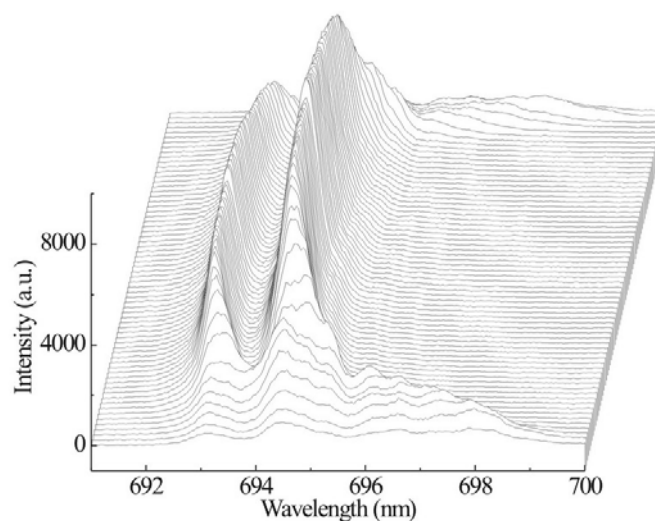


Fig. 3-15. A series of ruby fluorescence spectra recorded along the loading axis from one contact to the opposite contact.

A sequence of spectra along the loading axis were recorded at a load of ~ 4 N (Fig. 3-15). Spectra in the middle of the series are of the normal shape because here the external load is distributed over a large area and the stress is several magnitudes lower than at the contact region. Moving from center to both ends, the spectra show clear decrease in intensities and the shifted peaks appear. The shifted peaks first show up as small shoulders on the right. Then they become distinctly separated and shift further to the right. Accompanying the shifting of peaks, there is also a broadening of the peaks. This might be caused by the variation of stresses within smaller domains inside the optical detecting volume. It implies the formation and distribution of numerous micro domains in a single crystal under stress.

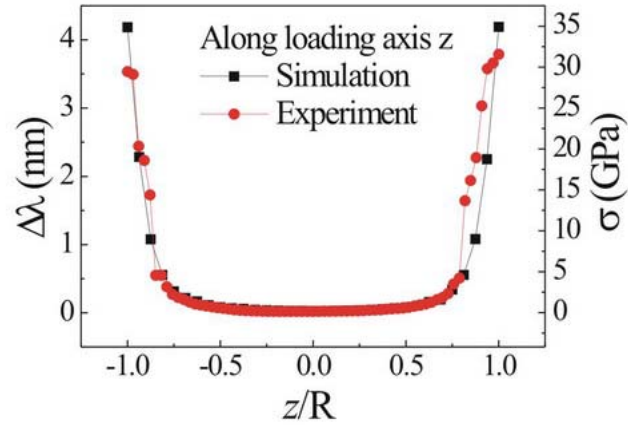


Fig. 3-16. Experimental data (red circle) is compared with simulation (square) along the loading axis. R is the radius of the ruby sphere and z/R represents positions along the z -axis.

The spectral shifts in Fig. 3-15 are compared with the values from simulations (Fig. 3-16). Measured values are in good agreement with simulations. However, at the contact region the experimental result shows lower stress values than in the simulations. In the vicinity of the contact region, i.e. $\sim 15 \mu\text{m}$ range, the experimental curve is less smooth and in some parts within this range the slope of the experimental curve is smaller than that of the simulation curve. This indicates non-elastic response and discontinuous behaviors in the contact region. In the following chapter, more detailed investigation of the contact region will be given together with quantified comparison with theoretical predictions.

3.5 Stress distribution at the microcontact

Although within the sphere the stress distribution is given by a complicated expression, in the contact area for frictionless and for a non-adhesive contact (which is a quite accurate description of my system) it reduces to the simple hemispherical stress profile [82, 83]

$$\sigma = P_0(2 + 2\nu)\sqrt{1 - (r_c/a_c)^2} \quad (1)$$

for the total stress. Here, P_0 is the maximal pressure along the loading axis in the center of the contact, and a_c is the radius of the contact circle. The contribution in normal direction is [84]

$$\sigma_z = P_0\sqrt{1 - (r_c/a_c)^2} \quad (2)$$

The integration of σ_z can be used to calculate the external loading force on the entire contact area:

$$F = \frac{2}{3}\pi a_c^2 P_0 \quad (3)$$

For the direct evaluation of the experimental data, Eq. (1) can be rewritten by substituting the maximal normal pressure P_0 for the maximal spectral wavelength shift $\Delta\lambda_0$:

$$\sigma = \frac{\Delta\lambda_0}{0.12(nm/GPa)}\sqrt{1 - (r_c/a_c)^2} \quad (4)$$

Equation (1) predicts a parabolic stress profile across the contact interface between the plate and the sphere. The prediction can be confirmed by comparison with experimental data (Fig. 3-17). Stress profiles of four contact areas of two spheres are plotted together in order to give a good statistics. The left y-coordinate is the wavelength shift and the right one is the total stress. When going across the diameter of the contact area, the stress distributed close to a hemisphere as predicted in Eqs. (1) and (2) [81]. By fitting the stress profiles measured at a load of ~ 4 N, I obtained $P_0 = 12.7 \pm 0.6$ GPa and $a_c = (11.2 \pm 1.0)$ μm , as indicated by the dashed line. The errors mainly come from the uncertainty of the maximum wavelength shift

$\Delta\lambda_0$ and the fitting process. The curves make a general impression that the left half is more regular a parabola than the left half. This could be caused by some systematic misalignment, for example, slight tilting of the stage above the objective lens, etc.

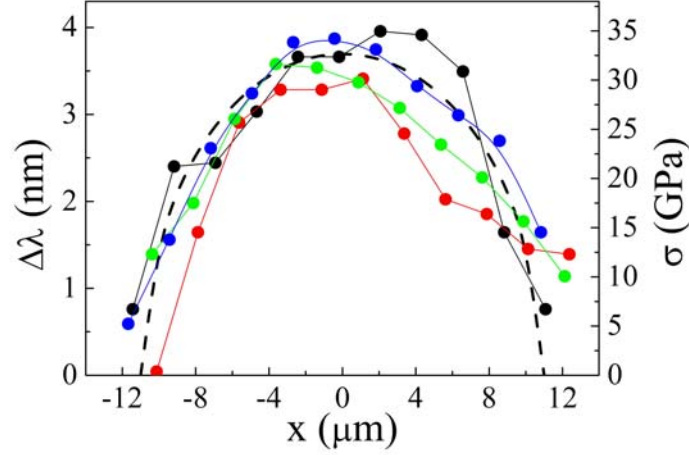


Fig. 3-17. Profiles of stress distributions along the x coordinate (Ref. Fig. 3-16) are plotted for the contact areas of four samples. The total stress in the contact area (right scale) was obtained by $\sigma = \Delta\lambda / 0.12$ (nm/GPa). The continuous dashed line is a fit with $\sigma = \frac{\Delta\lambda_0}{0.12} \sqrt{1 - (r_c/a_c)^2}$ using $a_c = 11.2 \mu\text{m}$ and $\Delta\lambda_0 = 3.8$ nm.

The results can be compared with values calculated with Hertz theory, assuming purely elastic response [84]. Using

$$a_c = \sqrt[3]{\frac{3R(1-\nu^2)F}{2E}} \quad (5)$$

and taking a load of $F = 4 \pm 0.3$ N, a contact radius of $(10.9 \pm 0.2) \mu\text{m}$ is calculated and $P_0 = (16.1 \pm 0.7)$ GPa can be obtained by Eq. (3), with errors assumed mainly to come from the uncertainty in the external load. Thus, within the error the measured values for P_0 and a_c generally agree with the calculated ones. With 12.7 GPa the experimental value is lower than the calculated pressure of 16.1 GPa, which is an indication of the onset of non-elastic deformation.

A set of stress profiles is obtained with different depth into the ruby sphere under a load of about 4 N (Fig. 3-18). All data points of the same curve are taken at a fixed depth beneath the contact interface. The top curve represents the profile of the

stress across the interface between the pressing plate and the ruby sphere. The following curves downwards are recorded inside the bulk of the sphere $\sim 4 \mu\text{m}$ interval to one another so that the bottom curve represents the stress profile about $15 \mu\text{m}$ beneath the contact.

The profile curves decrease in magnitude of stress one after another from top to bottom. The spacing between the curves near the top is smaller than near the bottom. Not all curves display hemispherical shape. Some show a broad plateau in the middle. It might indicate the onset of non-elastic response at a subsurface location beneath the contact. On the other hand, since I did not have infinitely small optical detecting volume and due to the effect of multi-scattering, some of the shifted peak appearing as a shoulder can only be vaguely determined. This could be a major source of errors.

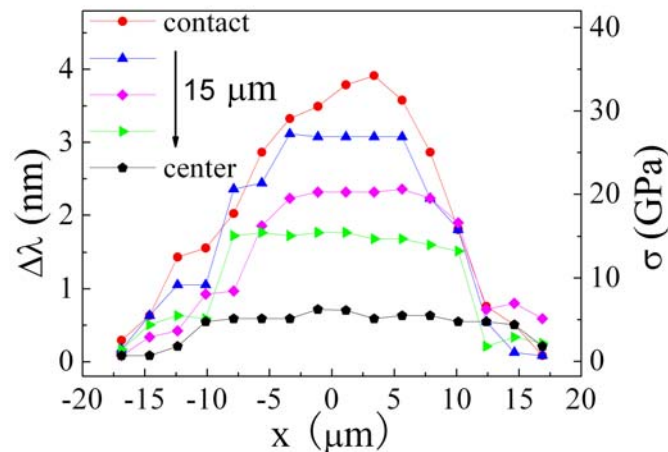


Fig. 3-18. A set of stress distribution profiles from contact interface into the bulk of the sphere beneath the area within the contact circle. Loading force $\sim 4 \text{ N}$. The spatial interval between each pair of curves is about $4 \mu\text{m}$.

Close to the contact, the highest wavelength shift of $\sim 4 \text{ nm}$ was observed, which corresponds to a total stress of $33\text{-}34 \text{ GPa}$ when the conversion factor 0.12 nm/GPa is used. The stress decreases steeply when going from the contact toward the inside of the sphere. The high stress region extends from the contact interface into the bulk of the sphere for about $1/5$ of the radius R . At about $15 \mu\text{m}$ from the contact the stress is already reduced below 20% of the maximum, around 5 GPa .

These results agree with simulations (Fig. 3-16).

Simulation results obtained under the assumption of pure elastic deformation are compared to the experimentally measured stresses (Fig. 3-19). In the experimental contour, the high stress domains extend to broader region in the horizontal direction and patches of bluish color appear at the corners. The change of the color from red-yellow (higher stress) to green-blue (lower stress) is sharp. While in the simulation contour, the color gradient is smoother and red-yellow color, indicating high stress, extends deeper into the bulk beneath the contact interface in the vertical direction. The sum of stress from both contours are of the same level but in the experiment the transmission of stress is shorter and shaper. I interpret this as a sign of non-elastic deformation.

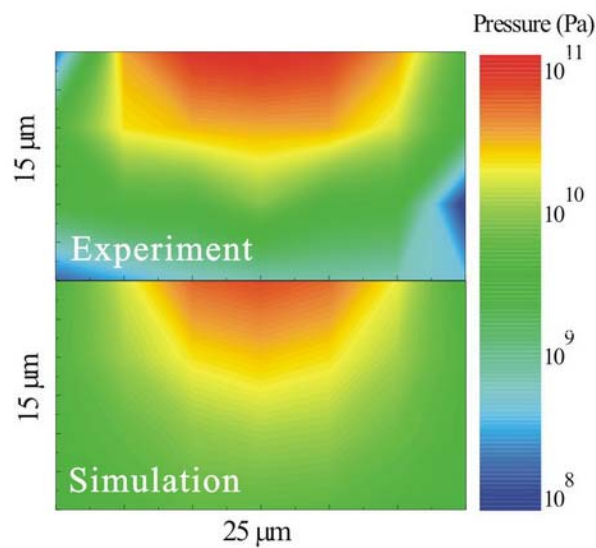


Fig. 3-19. Contours of stresses in the vicinity of the contact region. A range of 15 μm from the contact into the bulk of the ruby sphere has been shown.

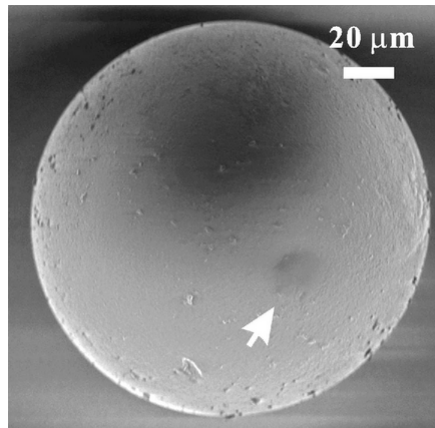


Fig. 3-20. SEM image of a ruby sphere after applying a load of ~ 4 N between two sapphire plates illustrating the permanent deformation of the contact area after compression.

The SEM image (Fig. 3-20) shows a weak but clearly visible dark circle at the contact area (indicated by the arrow). This dark area has a radius about $9.5 \mu\text{m}$, $\sim 15\%$ smaller than the calculated radius of the contact area. This is reasonable because the rim of the contact area is under stress below the critical value that causes permanent deformation.

The permanent impression indicates either plastic deformation or the formation of microcracks. In the case of plastic deformation, one expects a uniform stress value within certain region around the contact point. While in the case of formation of microcracks, one expects decreased stress values and less regular stress distributions. The experimental results hint to the second interpretation. But based on these results alone no clear distinction can be made. Therefore, I measured the change of stress at a given position in the contact region when increasing the load. This will be discussed in the coming chapter.

3.6 Quasi-static compression and stress development

To study the development of stress as well as determine the yield stress in the contact region, I increase the load stepwise using the step motor while monitoring the shift of fluorescence spectra.

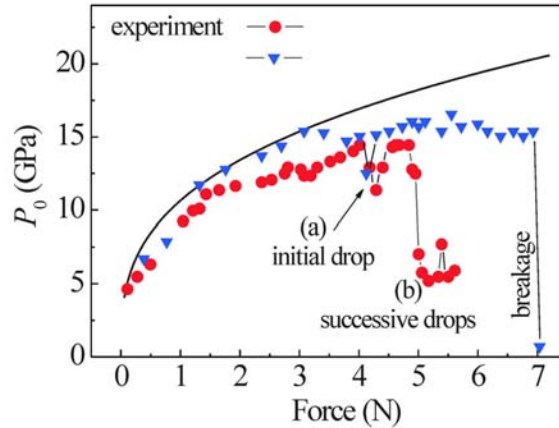


Fig. 3-21. Experimental maximal pressure P_0 on the loading axis measured as close to the contact as possible. Results of two representative experiments are shown (●, ▼). For comparison calculated values are plotted (continuous line).

Experimental pressures measured during the loading process in the center of the contact area are compared to the calculated values (Fig. 3-21). The symbols (●, ▼) are the results of experiments with two different spheres representing two types of behavior. The continuous line is the maximal pressure P_0 calculated with Eqs. (3) and (5). When the loading force is below 2 N, corresponding to a vertical stress of 12-13 GPa, experimental and theoretical results generally agree with one another and the deformation of the sphere is supposed still within the elastic range. Within 2-4 N, however, the deviation between calculation and experiments becomes larger. I take this as the range within which non-elastic response, e.g. formation of microcracks, starts to occur. Non-elastic deformation sets in when the shear stress component of the Hertzian stress field reaches one half of the yield stress Y . The shear stress has a maximum value of $0.47 F/\pi a^2$ at a subsurface location along the contact axis [1]. The yield

stress is related to the hardness H by $H \approx 3Y$ [72]. Together with Eq. (5) these equations lead to a critical load F_c for the onset of non-elastic deformation given by

$$F_c = \left(\frac{\pi}{2.8}\right)^3 \left[\frac{3(1-\nu^2)}{2}\right]^2 H \left(\frac{HR}{E}\right)^2 \quad (6)$$

Inserting $H = 25 \pm 5$ GPa, $\nu = 0.25$, $E = 350$ GPa, and a radius of the sphere of $R = 75 \mu\text{m}$ the critical load is $F_c = 2.3 \pm 1.2$ N. Therefore it is expected that above 2 N the deviation between measurement and calculation occurs.

Above the non-elastic regime and before the final failure of the sphere, two typical stress curves have been observed. In one case (shown by curve of $|\bullet|$), more than one sudden decrease in pressure was observed. Between loads of 4-5 N the pressure typically decreases discontinuously by $\approx 10\text{-}25\%$, which I interpret as a sign the coalescence of microcracks. At this load the sphere does not macroscopically break. When the force is further increased, the stress recovers to the level before the initial drop of stress but seldom exceeds. After some more loading, successive sudden drops of stress typically take place at a load of 5-6 N. This time, the pressure decreases more and the contact area is supposed to subject to another crack, likely of larger scales. After the major crack, the pressure did sometimes rise to a higher value but rarely to the level before.

In the other typical case (shown by curve of $|\blacktriangledown|$), the sudden drop of stress also usually occurs in between 4-5 N and then recovers to the level before the drop of stress. There is no obvious trend of pressure increase after the first crack when further increasing the load. A few small fluctuations on the curve imply that local stresses go up and down at some tiny regions. (It has something do to with the distribution and evolution of these micro stress domains under compression and will be discussed later in the experiment of vibration loading.) Since the load increases while the stress does not, it indicates increase in the contact area and continuous redistribution of the stress bearing domains within the contact circle. When further increasing the load, the ruby sphere broke catastrophically at loads of typically 6-7 N

or at the pressures P_0 of 14-15 GPa in equivalence.

Applying Trescas criterion [1], $P_0 \leq 2Y$, where Y is the yield strength in the contact area. With $Y = 8-12$ GPa [51, 85], the experiments are at the verge from elastic to non-elastic response of ruby.

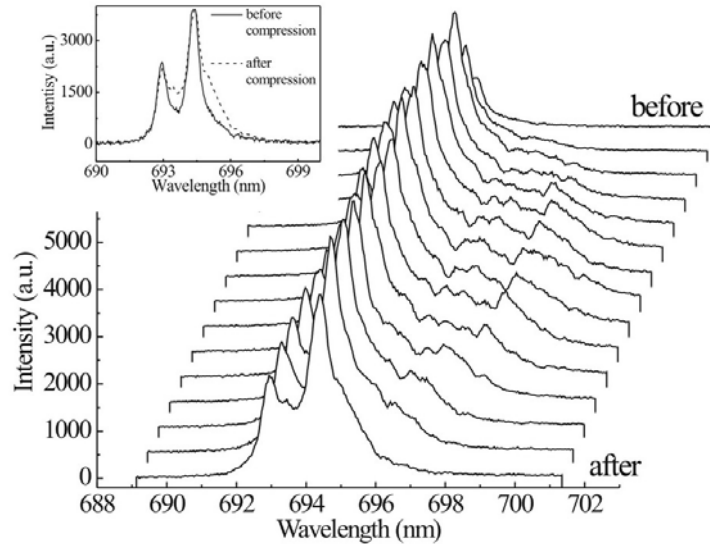


Fig. 3-22. A sequence of spectra in which the loading force is first increased and then decreased (in sequence top to bottom). Inset: Difference between spectrum at zero load before and after the loading cycle.

Permanent deformation of a ruby sphere, which has been exposed to a load above 4 N, is verified by examining a relaxed sphere after compression. Figure 3-22 shows a series of spectra recording the process of loading and unloading. The middle curve represents the highest loading force. Comparing the upper and lower half of the series, it is found that during decreasing of the load the stress is lower than during increasing of the load. This is the evidence of inelastic response. Non-elastic deformations lead to an increase of the contact area so that the load can be counterbalanced. When unloading, the contact area does not reduce accordingly and this results in lower of stress values. The bottom spectrum shows a small peak between the two main R lines and a small shoulder to right of the R_1 line. These are

the shifted peaks due to the residual stress. It also indicates tiny granules might form at the contact region resulting from the non-hydrostatic compression, which holds the residual stress even when the external load is completely removed.

The hysteresis of stress curve between loading and unloading processes is shown in Fig. 3-23. The stress curve of loading increase smoothly while the curve of unloading has a turning on its lower part. Before the turning the unloading curve is below the loading curve, showing a faster decrease in stress due to enlarged contact area. After the turning point the unloading curve decreases less sharply and finally sits upon the loading curve, indicating the residual stress at the non-elastically deformed contact region.

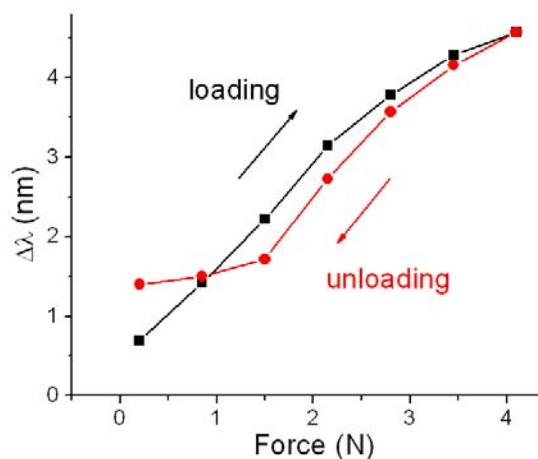


Fig. 3-23. Hysteresis of stress within a loading and unloading cycle.

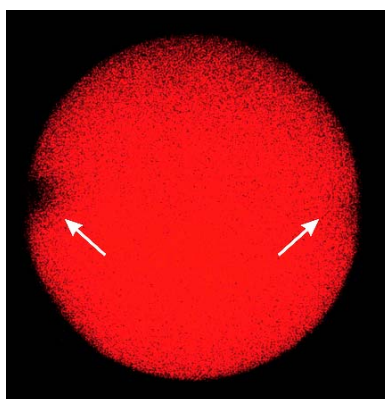


Fig. 3-24. Fluorescence images of ruby sphere being loaded from left and right.

Sometimes the stress changes inside the ruby sphere can also affect the fluorescence intensities on the laser scanning images. Figure 3-24 is the fluorescence

image taken during one experiment, in which a sphere was compressed at left and right with a load of 4-5 N. The highly stressed regions close to the contact points as indicated by the two white arrows have much weaker intensities compared with the rest parts. Though the effect of quenching should happen when ruby is subjected to much higher stresses than in this experiment, the weakening of intensity might also indicates certain changes of the environment round fluorescing sites near the contact points.

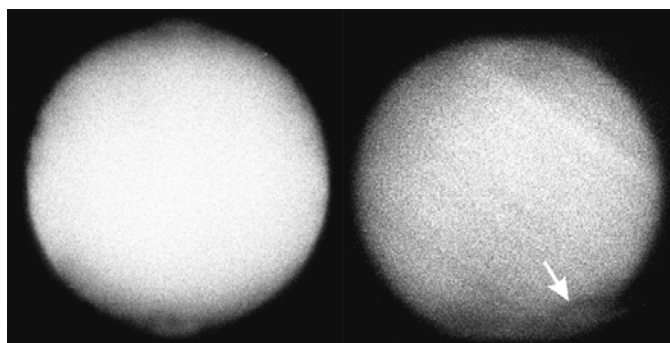


Fig. 3-25. Fluorescence images of ruby sphere without load (left) and at a load of 5.5 N (right) just before breaking (contrast increased).

In another case a fluorescence image was recorded just before the failure of a sphere (Fig. 3-25). The picture on the left is the typical fluorescence image of a ruby sphere before compression. It is clamped from top and bottom. The right image is the sphere at the threshold of breakage. On the right image, the sphere shows bright and dark stripes of the about 135° . This indicates that the high stress at contact region is transmitted throughout the whole sphere and changes of fluorescence intensity along certain crystallographic direction. It might be caused by tiny deformation or twisting of the crystal lattices under high pressure. At the bottom of the sphere on the right one can see the flattened contact region along with much weakened fluorescence intensities. The white arrow also indicates the formation of a crack on one side of the contact region.

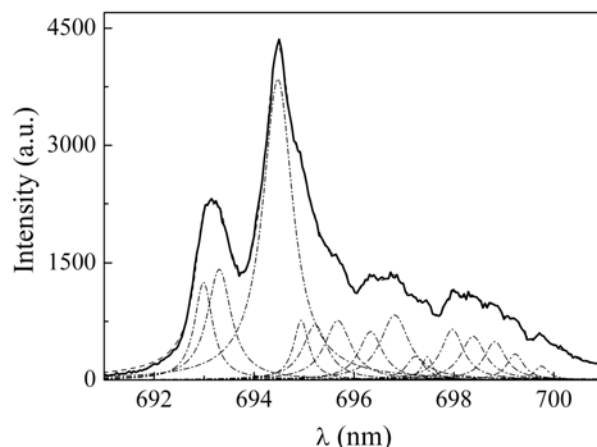


Fig. 3-26. An experimental fluorescence spectrum recorded at the contact point of a ruby sphere under a load of ~ 4 N. 16 Lorentzian peaks are used to fit the experimental curve.

Looking into details of spectra in figures 3-13(d) and 3-22, a general feature is noticeable, i.e. most curves show zigzag topography or multi-peaks. An experimental spectrum is fitted with 8 sets of Lorentzian double peaks (Fig. 3-26). I take this as evidence that within the detecting volume of $\approx 2^3 \mu\text{m}^3$ discontinuous domains exist. Within each domain the stress may be homogeneously distributed but different domains bear different stresses. These domains share the total external load and together give the experimental spectra.

The resolution I have until now does not allow finer characterization of these micro domains. A better resolution is required for a smaller detecting volume as well as for eliminating the background due to multi-scattering. Therefore, two-photon excitation is tested and used for the following studies.

3.7 Two-photon excitation

In order to improve resolution as well as to reduce the background, I tested two-photon excitation in comparison with one-photon excitation.

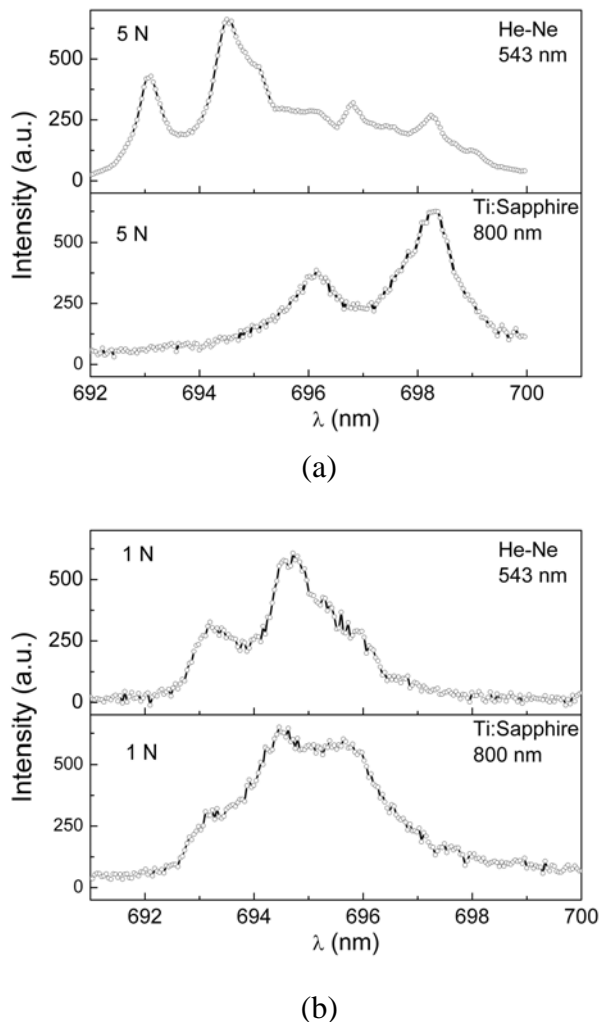


Fig. 3-27. Comparison ruby fluorescence spectra taken with one- and two-photon excitation at the contact areas by switching between He-Ne laser (543 nm) and Ti:Sapphire laser (800 nm).

With He-Ne laser excitation, intensive background appears on the left side of a spectrum. For the spectra under high load (Fig. 3-27a, upper panel), the multiple peaks usually accompany one-photon excitation. At low load (Fig. 3-27b, upper panel), the shifted peaks sometimes submerge into the background. Because of existence of intensive background, when going through a whole series of spectra with increasing load, one easily gets a disillusion that the peaks simply rise from

certain positions rather shifting continuously, while the original double peaks remain still.

With the two-photon excitation, the determination of a shifted peak becomes much easier (Fig. 3-27a, lower panel), even at a quite low load (Fig. 3-27b, lower panel). In two-photon excitation, the probability of emission is much lower. It is only possible to excite at the tip of the light cone, which leads to a high resolution and an enhanced detection depth (Fig. 1-17).

A series of ruby fluorescence spectra recorded along the loading axis with a high load of 4-5 N is shown in Fig. 3-28. Figure 3-28(b) is the normalization of the spectra in 3-28(a) for a better display. Comparing to Fig. 3-15 in section 3.4, here the spectra near the contact regions (top and bottom) show much clearer shifted peaks. In addition, there is almost no noticeable background.

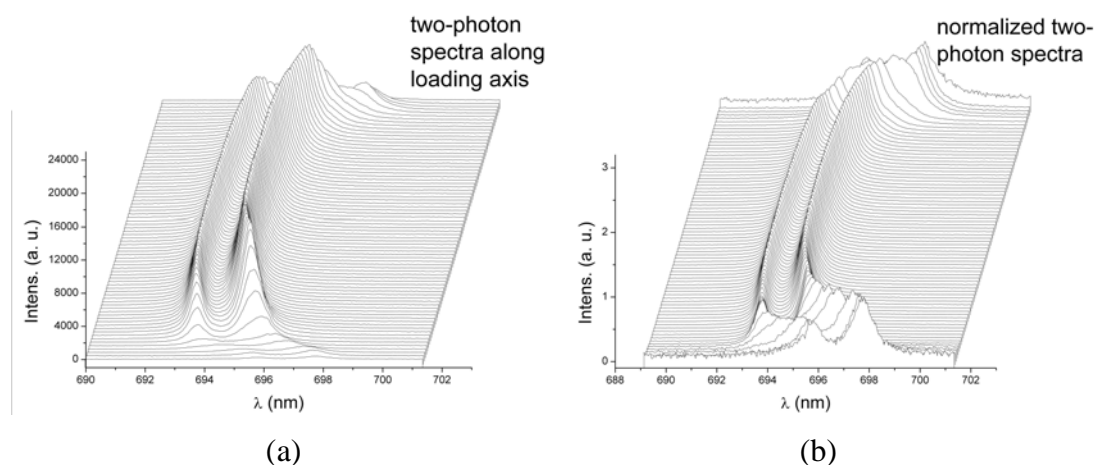


Fig. 3-28. (a) A series of spectra recorded along the loading axis using two-photon excitation (Ti:Sapphire laser, wavelength 800 nm); (b) the same series of spectra along the loading axis are normalized to show explicitly spectral shifts.

Looking at the spectrum of two-photon excitation in Fig. 3-27(b), it seems there is still significant background on the left side. However, the following experiment gives an opposite answer.

In the experiment, a series of spectra were taken when the loading force was first increased from 1 N to 4 N and then decreased back to 1 N. The top and bottom

spectra were taken at low stress. Instead of having two peaks, they show a shoulder on the left. This shoulder seems to represent the remaining background. However, when the load increases, the left shoulder decreases. When reaching the highest load of 4 N, the shoulder disappears almost completely. According to this observation, the small peak on the left of the spectra at low stress (Fig. 3-27b) should be the light from within the laser focus. Moreover, the evidence of different stress domains exist within the small detecting volume is in this case more concrete.

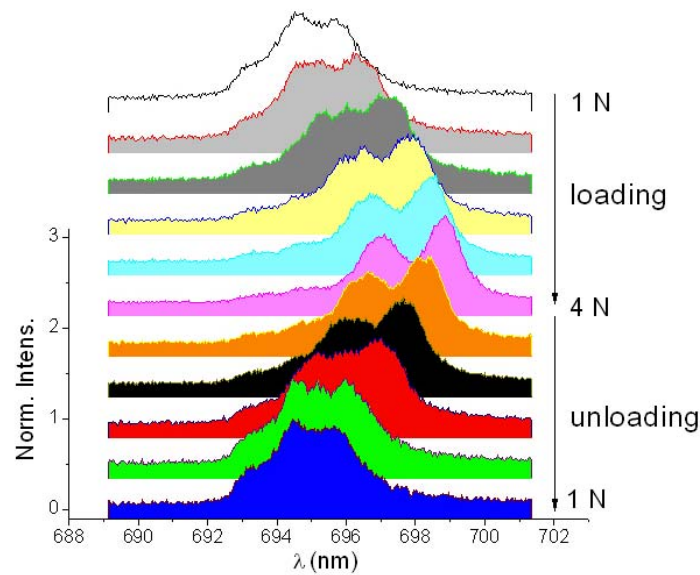


Fig. 3-29. A series of ruby fluorescence spectra taken at the contact area during a loading-unloading cycle with two-photon excitation.

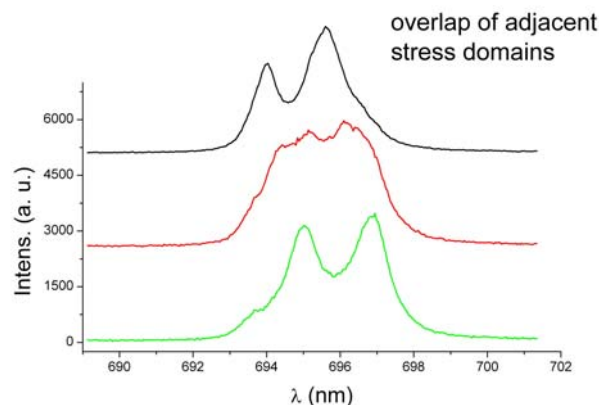


Fig. 3-30. Three ruby fluorescence spectra along the loading axis 2 μm away from each other. The load is 4-5 N and two-photon excitation was used.

Using two-photon excitation, it is also possible to detect the boundary between different domains. Three fluorescence spectra adjacent to each other with spacing of 2 μm are shown in Fig. 3-30. The middle spectrum is broadened and shows multiple peaks. It seems to be the superposition of the top and bottom spectra. According to the experiment of Fig. 3-29, each spectrum contains information only within the laser focus. Therefore, the middle spectrum indicates two discontinuous stresses within the optical detecting volume, which sits on the boundary of adjacent domains. It implies the possibility of detecting the micro domains within the ruby crystal.

According to the above results, two-photon excitation successfully eliminates most of the background and largely reduces the effective optical detecting volume. With a smaller detecting volume ($\sim 1 \mu\text{m}^3$) and low background, two-photon excitation allows observing distinct wavelength shifts within the whole reachable range of stresses.

3.8 Repeated loading cycles

To study the contact fatigue of ruby, repeated loading-unloading cycles are applied to the sphere. The procedure is as the following (Fig. 3-31): the loading force is first gradually increased with step increments of 0.055 N to a maximal load of 1.1 N and then gradually lowered to zero again. At each step it takes 5 s to record a fluorescence spectrum. Afterwards the load is increased to 2.2 N, decreased to zero, increased to 3.3 N, etc. For the last cycle, the maximum load is often off the pre-determined values, since in this cycle failure of the contact area occurs so that the loading process is usually held until the ultimate drop of stress.

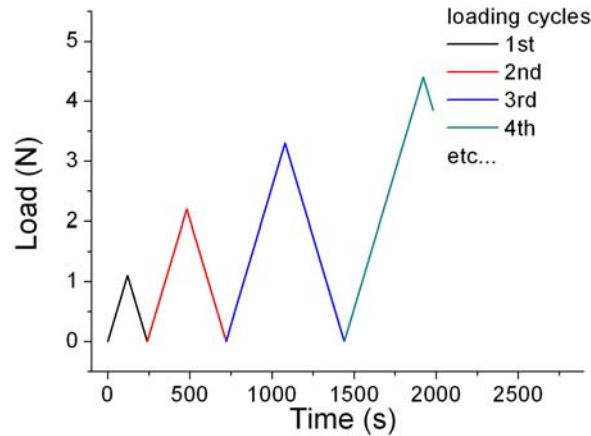


Fig. 3-31. The experimental procedure of the repeated loading-unloading cycles.

With the above procedure, a set of typical stress-vs-load curves recorded at the center of the contact area is usually recorded (Fig. 3-32). The measured curves can be compared with calculations. Putting Eqs. (1), (2), (3) and (5) together, the total stress can be related to the load. In the center ($a_c = 0$)

$$\sigma = \frac{3}{\pi} (1 + \nu) \cdot F^{1/3} \cdot \left[\frac{2E}{3R(1 - \nu^2)} \right]^{2/3} \quad (7)$$

The stress-vs-load curves show a dependency as $\sigma \propto F^{1/3}$. For the first cycle the Young's modulus of 340 GPa agrees with literature (350 GPa). Since the second

cycle the stress-vs-load curves are at lower stresses than the previous one. This is a sign of fatigue, which brings continuous damage to the contact area.

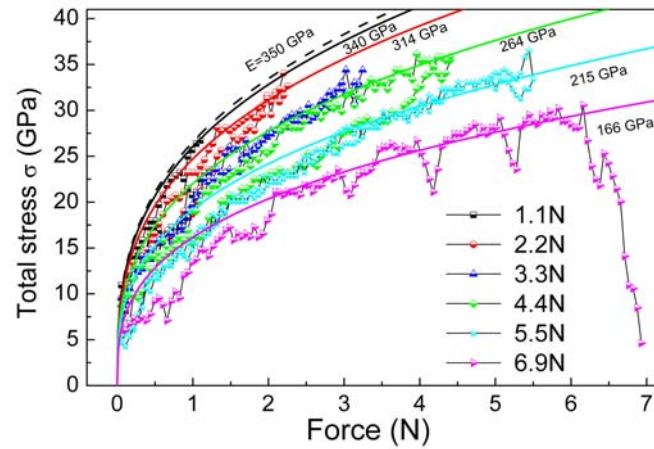


Fig. 3-32. A series of stress-vs-load curves that are recorded during cyclic loading-unloading procedures. The maximal loading force is increased for each next cycle and the values are as the inset column of numbers. The lines were calculated using Eq. (7) with Young's moduli of $E = 340, 314, 264, 215,$ and 166 GPa, and Poisson ratio of $\nu = 0.25$.

All stress-vs-load curves are fitted reasonably well with Eq. (7), but reduced effective Young's moduli have to be inserted (the influence of Poisson's ratio is less important). The effective Young's modulus decreases to 314 GPa at a maximal load of 2.2 N, and 264 GPa when increasing the load to 3.3 N. The same Young's modulus can be used to fit the increasing load branch of the next cycle up to 4.4 N. At 4.4 N the stress decreases so that the decreasing curve agrees with an effective Young's modulus of 215 GPa. 215 GPa also fits the next loading cycle up to 5.5 N. The last cycle, which goes up to breakage at 6.9 N shows an effective Young's modulus of 166 GPa.

To quantify fatigue I calculate the damage. In the continuum model the damage D is the reduction in load carrying effective area [37, 86-88]. The continuum model was originally developed to describe fatigue in brittle, heterogeneous materials, such as concrete. I related damage to the effective Young's modulus E^* (assuming constant

Poisson ratio) by $E^* = E(1 - D)$ [37]. D is here the fractional reduction in elasticity, being zero for the undamaged sphere and one when the sphere has no remaining stiffness. In the experiment, damages are $D = 0.076$ (2.2 N load cycle), 0.22 (3.3 N), 0.37 (after 4.4 N), and 0.51 (6.9 N), respectively.

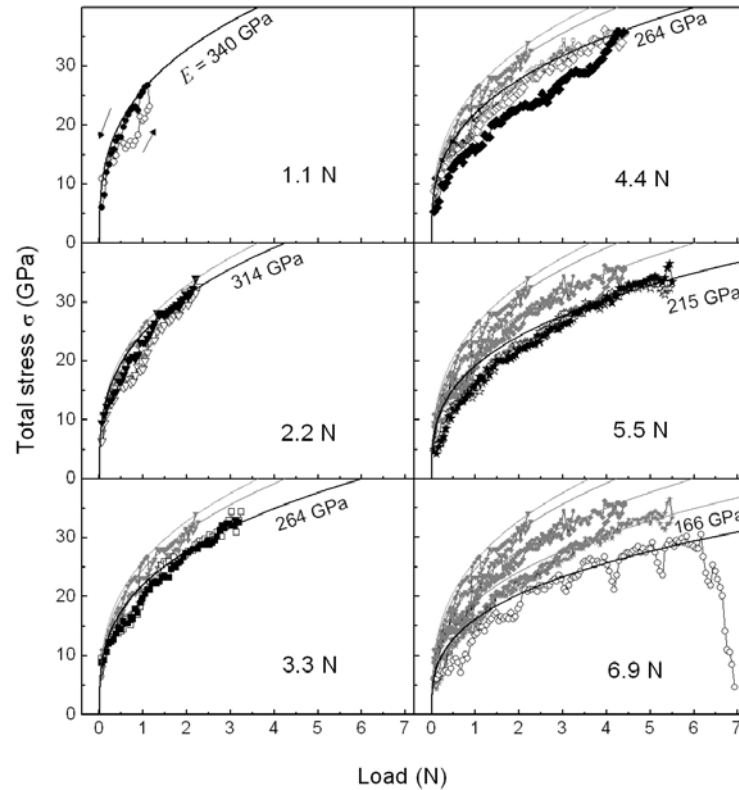


Fig. 3-33. The stress-vs-load curves from Fig. 3-32 are plotted in a stepwise manner. Open symbols indicate the increasing load; filled symbols correspond to decreasing load.

After discussing the overall shape of stress-vs-load curves, I would like to point to deviations. The separate steps of the loading cycles are shown as a sequence in Fig. 3-33. On the first few increasing load cycles (1.1 and 2.2 N) the stresses are slightly lower than on the decreasing curve. This can be attributed to surface roughness. Initial contact between the sphere and the plate is established at asperities, which have a much smaller radius of curvature than the radius of the sphere. As a result the real contact area at initial contact is much smaller when predicted by Eq.

(5). When increasing the load the non-elastic limit in the asperities is reached and they are deformed, showing decreased stresses.

For intermediate loads up to 3.3 N the deviation between increasing and decreasing curves is negligible. When going to 4.4 N or higher usually the increasing curve showed higher stress than the decreasing curve. This is an indication of entry into the non-elastic phase [89]. This separation starts at the beginning of unloading from 4.4 N. The unloading curve of the fourth cycle almost superposes with the curve of the following loading to 5.5 N.

In the sixth loading process, a sequence of spike-like decrease (drop) of stress occurs. It indicates the coalescence of micro-cracks and the shift in the load carrying regions. These spikes are in periodicity except the first drop that occurs at a load about 0.7-0.8 N. Taking the increment of loading force as measurement, the periodicity is around 1 N. Above 6 N the decreased stress shows a short rise followed by a significant drop. This indicates the breakage of the whole contact area [89]. The sudden decrease or the drop of stress most likely correspond to discontinuities or “Pop-ins” observed in indentation experiments on sapphire [90, 91]. These pop-ins have been attributed to a twinning process in the high strain rate deformation [92].

To estimate the accuracy and reproducibility of the stress measurements, loading and unloading stress curves from successive cycles are compared (Fig. 3-34). The upper panel shows the first loading cycle up to 1.1 N maximum and the lower panel is the second loading cycle up to 2.2 N maximum. In the first cycle, the loading curve sits above the unloading curve and they form two bubbles. The features reappear on the second loading cycle at the same ranges of loads and with similar shapes. Looking into the details, one can see that the small rise at the load about 0.7 N on the unloading curve of first cycle also occurs on the unloading curve of the second cycle. The precise reproduction of features in two different cycles convinces that the spatial steadiness of the laser focus is good. Therefore, the experimental procedure is reliable concerning accuracy of measurement.

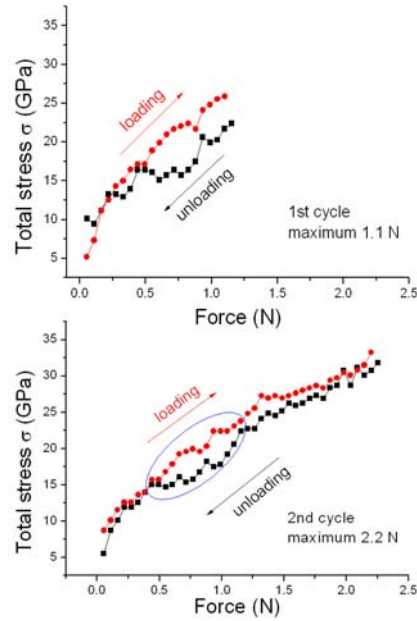


Fig. 3-34. Loading and unloading curves of the first and second loading cycles with maximal loading force 1.1 N and 2.2 N, respectively. The blue oval ring indicates the similarity of the two cycles at the same loads.

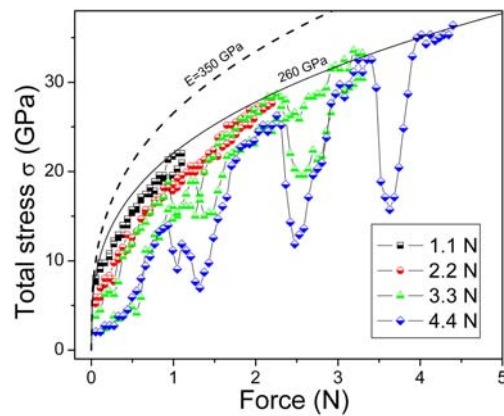


Fig. 3-35. A second series of stress-vs-load curves that are recorded during cyclic loading-unloading procedures. The maximal loading force is increased for each next cycle and the values are as the inset column of numbers. The lines were calculated using Eq. (7) with Young's moduli of $E = 340$ GPa and 260 GPa, Poisson ratio of $\nu = 0.25$.

A second representative result was obtained with another sphere using the same procedure (Fig. 3-35). The dashed line is the theoretical stress curve calculated

with Eq. (7) with Young's modulus $E = 350$ GPa and the continuous line is the calculation with $E = 260$ GPa.

The whole bunch of curves show deviation away from the calculated line with $E = 350$ GPa, though no contact damages should be expected before the first loading starts. It could be partially caused by the variation of the mechanical property for different ruby spheres or could also be affected by the crystallographic orientation with respect to the loading axis, since ruby crystal is an anisotropic material.

In general, each curve moves to lower stress values compared to the curve in the previous cycle. However, the top stress value at the end of each curve sits on the same line fitted by Eq. (7) with a reduced Young's modulus $E = 260$ GPa. If the material inside the laser focus undergoes permanent damage, the stress should not keep rising with the increasing external load. Therefore, I suggest the following: The material within the laser focus is generally within elastic range during the four cycles of loading. But some continuously enlarged damage that occurs elsewhere from the laser focus (most probably at a subsurface location beneath the contact area) may be expected. On the other hand, propagation of microcracks and their coalescence again happen inside the contact area, as implied by the spike-like decrease of stress.

The separate steps of the loading cycles are shown as a sequence in Fig. 3-36. In the first cycle up to 1.1 N the loading curve lies under the unloading curve, which is attributed to the surface roughness as discussed in the previous experiment. In the second cycle up to 2.2 N the loading and unloading curves superpose each other quite well. This indicates the process is still within elastic range.

When increasing the load up to 3.3 N, spike-like sudden decrease of stress sets off. Two sudden decreases occur at 1.4 N and 2.5 N and also appear at the same loads when unloading from 3.3 N. The amplitudes, however, increased. It indicates more damages could have happened during the unloading process. Though for impact experiments, damage during unloading due to plastic solidification of the contact zone has been reported, the reason of damage during low speed, quasi-static

compressive unloading as in my condition is not clear.

On the loading curve up to 4.4 N, drop (sudden decrease) of stress occurs with even more increased amplitudes. At inverting from loading to unloading certain severe changes might have taken place so that the stress drops dramatically. This could be the sign of a permanent damage at larger scales. During unloading, fluctuations appear at the same loads where spike-like sudden decrease of stress has occurred before.

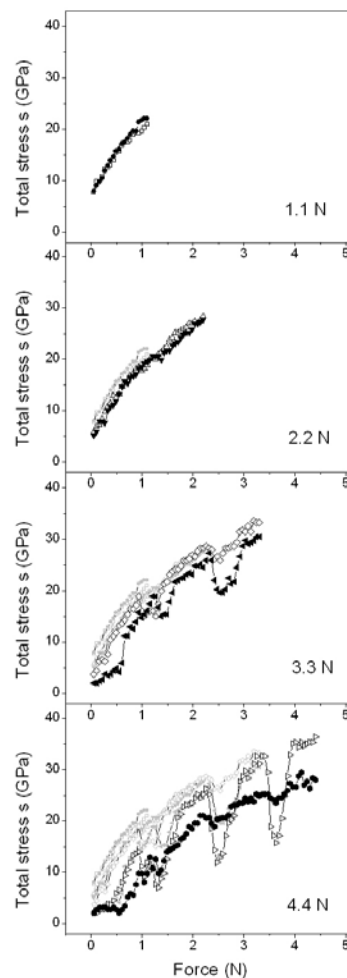


Fig. 3-36. The stress-vs-load curves from Fig. 3-35 are plotted in a stepwise manner.

Open symbols are used for increasing load and filled symbols for decreasing load.

Only loading curves from the above experiment are plot together in Fig. 3-37. The two black double-arrows point out the similar features on the two curves of the loading processes up to 3.3 N and 4.4 N, respectively. These features reproduce

themselves with high precision that the small jump at around 1 N and the kink at 2.8 N can be clearly observed on both curves, with proportionally enlarged magnitudes. Such “feature amplifying” indicates the accuracy of the measurements and the continuous changes of the local structure.

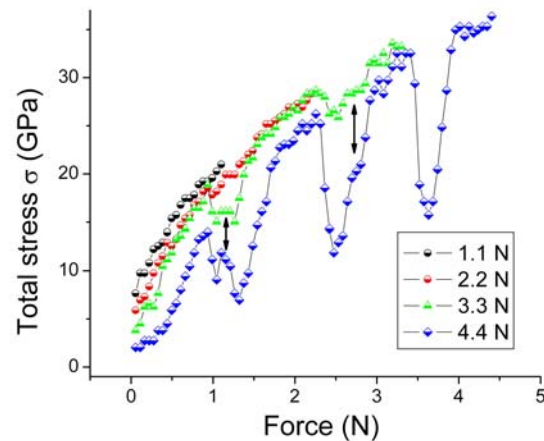


Fig. 3-37. Curves of only the loading processes from Fig. 3-35 are plotted. The black arrows indicate the shapes of the curves are retained with only difference of magnitude.

Like the two representative experiments shown in Figs. 3-32 and 3-35, the spike-like sudden decreases of stress have been reproduced in different experiments. The initiation of such stress decreases usually starts during the up-loading processes. Once initiated, they repeatedly occur at the same loads in the following cycles (also during unloading processes). The occurrences of sudden stress dropping take place at loads very close to loading-unloading inversions of the former cycles. Therefore, a possible interpretation is that each time at the inversion of loading to unloading under high stress, some structure change happens and results in a sequence of weak points. These weak points are recorded or “memorized” and reflected in the subsequent cycles as periodical sudden decreases of stress, when the material is above certain threshold of fatigue.

Based on the above observation, one of the possible mechanisms to the sudden decrease of stress is proposed: Disconnected parts separated by microcracks formed during the loading processes. They share the total load together. When

propagation or coalescence micro-crack takes place, local yielding or relaxing happens to some of these parts, leaving the rest parts to bear the load so that their stresses rise. When the load carries on, the inversed process happens. The load bearing parts undergo local yielding (or relaxing) and their stresses decrease again. Such course appears as the fluctuation on the stress curves.

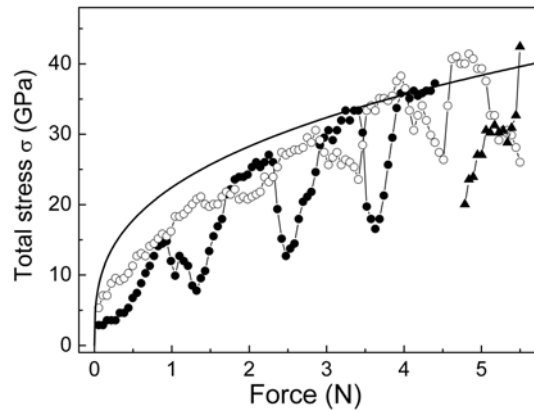


Fig. 3-38. Stress-force curves recorded in the same experiment at two different spots A and B, which were 10 μm apart but both still in the contact region. (●) Loading at spot A to 4.4 N. (○) Loading to 5.5 N at spot B. (▲) Unloading at spot A from 5.5 N. The continuous line is calculated with Eq. (7).

To verify this hypothesis I take advantage of two-photon excitation, since the exciting/detecting volume is so small that different parts within the contact region can be resolved in the same experiment (Fig. 3-38). Solid circles show the loading process up to 4.4 N at spot A. A was slightly off the center. Sudden decrease of stress has occurred during the loading. After unloading from 4.4 N to zero load the laser focus is shifted 10 μm away from A to B. Then the load is gradually increased to 5.5 N at spot B (open circle). Here, sudden decrease of stress is again observed with almost the same periodicity as for spot A, however, with a different sign. A stress decrease at A corresponds to a stress increase at B, and vice versa. After the maximal load 5.5 N has been reached, the laser focus is shifted back spot A to monitor the unloading process from 5.5 N, as shown by the short curve of triangles.

At 5.5 N, the stress at **B** is at a valley. Meanwhile, the stress at **A** is likely at the peak of a period. By unloading from 5.5 N, the stress at **A** decreases as expected. This justifies to certain extent the proposed mechanism.

3.9 Periodic loading using piezo vibration

Until now I have described experiments with static pressure, in which the loading processes are in stepwise manner and the recording of a fluorescence spectrum is under a constant load. In this chapter, I will present a different loading method: vibration loading. In which the load periodically oscillates at relatively higher frequencies while taking a spectrum.

The vibration loading was driven by a piezo. Since the approaching and fixing of the piezo to the pressing plate were done manually with the ruby sphere already clamped, there was a non-negligible initial touching force. In order to have an initial load as low as possible, I tuned the offset of the piezo so as to get an initial load of 0.1-0.5 N. This load was denoted by a wavelength shift of the R_1 peak to 696-697 nm. However, I could not quantitatively determine the precise initial load only by the wavelength shift. During the experiment the vibration frequency and displacement of the piezo were adjustable parameters. For data analyzing the shape of ruby fluorescence spectra was mainly concerned. I used vibration frequencies of 0.2, 1, 5, 10, 20 and 200 Hz and vibration displacement of the piezo up to 6 μm .

Figure 3-39 shows a set of spectra in an experiment using the same ruby sphere. Vibration loading was at 0.2 Hz with piezo displacement amplitudes of 3, 4, and 5 μm , respectively. At each displacement, one set of 20 curves was recorded during vibration with the exposure time of 5 s for a single curve. Each set of curves included 24 vibration cycles. Red curves were taken before vibration and blue curves after vibration when piezo displacement was 0. The starting R_1 peak was at about 697 nm.

For all the curves (Fig. 3-39) recorded under vibrating load, a four-peak shape rather than a single broadened large peak can be observed. This is partially due to the vibration function. The vibration of the piezo is a sinusoidal function. The duration time is longer at both maximum and minimum load than loads in between. Thus the peak intensities are increased at both ends.

In the sequence of the vibration displacement 3, 4, and 5 μm , the “shoulder”

on the right rises and becomes a distinct peak. The outer rim of the right side peak shifts to the longer wavelength ranges with increasing of the vibration displacement (Fig. 3-39d).

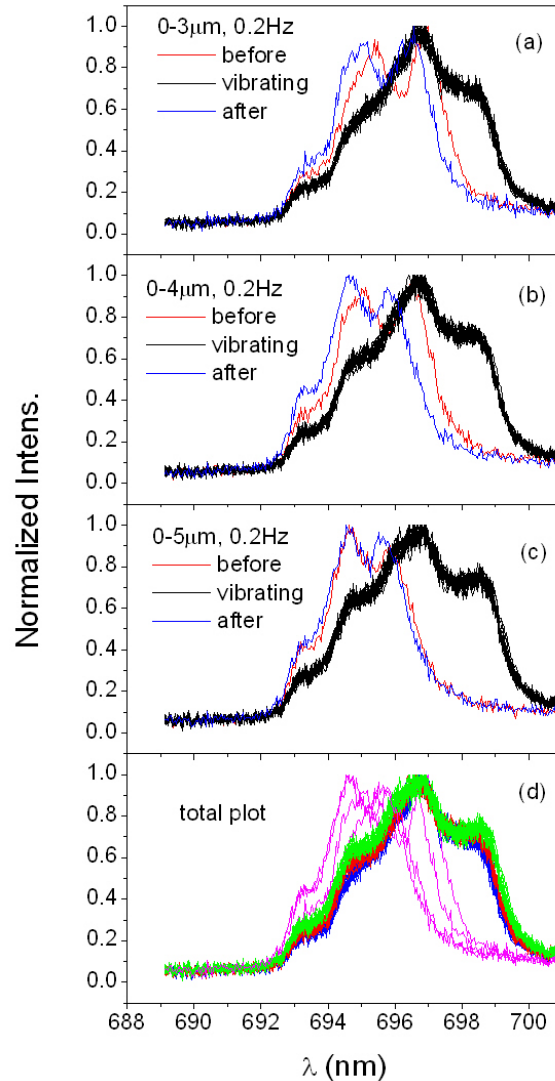


Fig. 3-39. Ruby fluorescence spectra were taken under vibration loading at 0.2 Hz with displacements of 3, 4, and 5 μm , respectively.

In the top two panels (Fig. 3-39), a distinct shift appears between the red and the blue curves. This is a sign of fatigue at the contact region. Thus the rising of the “shoulder” on the left can be attributed to the continuous damages and decreased elasticity. The shift between red and blue curves is smaller for Fig. 3-43c, though the displacement of the vibration increases by 25%. One possible explanation is that within a number of loading cycles the speed of damage decreases. It indicates that

continuous damages can only occur in such vibration loading to a certain limit, by which discontinuous behaviors, e.g. breakage, might follow.

A similar experiment (Fig. 3-40) was repeated with another ruby sphere. The vibration displacements were 1, 2, 3 and 4 μm , respectively. A frequency of 200 Hz was applied. The exposure time for taking one curve was kept constant as 5 s. For each displacement, a set of 20 curves were taken including 24, 000 vibration cycles. Red curves were taken before vibration and blue curves after vibration when piezo displacement was 0. The starting R_1 peak was at around 696 nm.

In Fig. 3-40(a) the spectra under vibration loading do not show a four-peak shape, because the vibration displacement is 1 μm and the high-stress peaks have not separated completely with the low-stress peaks. From Fig. 3-40(b) to 3-40(d) the right peak gradually becomes more distinct and shifts to longer wavelength range. The shifts get smaller with the increasing of vibration displacement, suggesting the maximum stress of elastic response has been reached. The trend of shifting is clear in the total plot in Fig. 3-40(e). In Fig. 3-40(d) only 7 curves under vibration were taken. Then the sphere broke abruptly. The noise-like blue curve shows losing of fluorescence.

The spectra at piezo displacement of zero (blue and red) shift gradually to shorter wavelength ranges. The trend is obvious in the total plot (Fig. 3-40e). Unlike in the previous experiment, this time they are much closer to each other. This is reasonable for two reasons. First, in this experiment the initial stress (peaked at 696 nm) is not as high as the former one (peaked at 697 nm). Second, the starting vibration displacement is only 1 μm . Thus the damages are smaller. Similarly, the distance of spectral shift decreases (Fig. 3-40c), indicating the speed of damage reduces after a number of cycles. However, during the same time the sphere is subjected to many more loading cycles so that the discontinuous behavior, i.e. the breakage, is accelerated (Fig. 3-40d). What is more, the spectra of zero displacement also show significant intensity decrease on the right side, indicating reduced domains of intact elasticity.

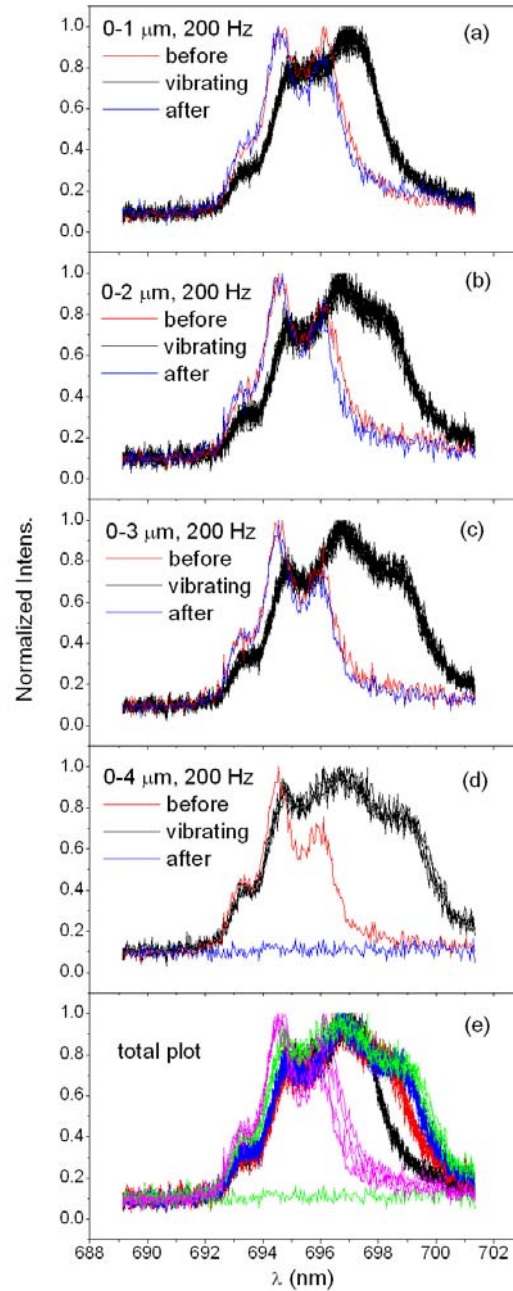


Fig. 3-40. Ruby fluorescence spectra were taken under vibration loading at 200 Hz with displacements of 1, 2, 3, and 4 μm , respectively.

The above two experiments used different frequencies. Though they differ from one another by a factor of 10^3 , the general trends of the damage are the same. Thus I conclude that the history of damage (fatigue) in vibration loading is dominated by the number of loading cycles. The fatal damages of discontinuous response, such as breakage, only occur when the vibration displacement

(corresponds to the magnitude of load) is above certain non-elastic threshold.

In order to study the effect of frequency in the vibration loading, I did the experiments, in which the displacement amplitude of vibration was kept constant and the vibration frequency was tuned.

In one of such experiment, the vibration displacement was set 5 μm . Different frequencies were applied as 0.2, 1, 5, 10, and 20 Hz, respectively. 20 curves were recorded for each frequency. The exposure time was kept 5 s for one curve. Each set of curves included 24, 120, 600, 1200, and 2400 vibration cycles, respectively.

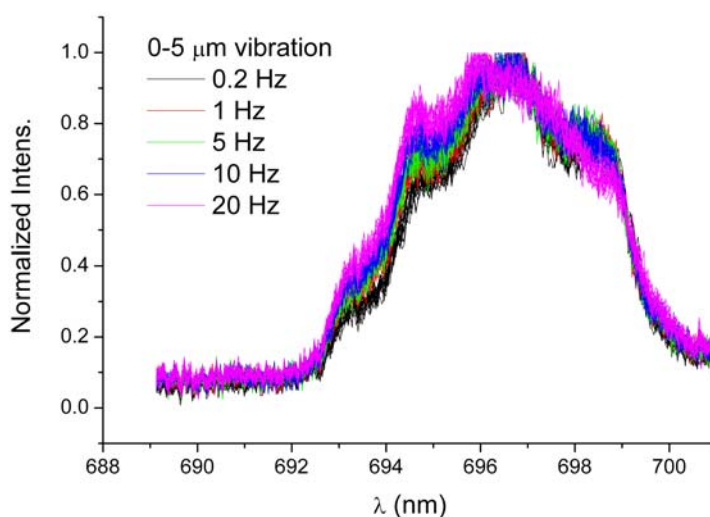


Fig. 3-41. Ruby fluorescence spectra were taken under vibration loadings with piezo displacement 5 μm and at frequencies 0.2, 1, 5, 10, and 20 Hz, respectively.

Normalized intensity values are used for the plot (Fig. 3-41). The intensity distribution over the whole spectra shifts from longer wavelengths towards shorter wavelengths with increasing frequency. The redistribution of intensity is not obvious until the frequency reaches 20 Hz, when a significant decrease of the right peak and increase of the left peak occurs. Meanwhile, the highest peak shifts to the left apparently. Such redistribution of intensity in the entire shape of the spectra indicates that inside the optical detecting volume domains of higher stresses decrease while that of lower stresses increase. It is also a measure of the remaining elasticity.

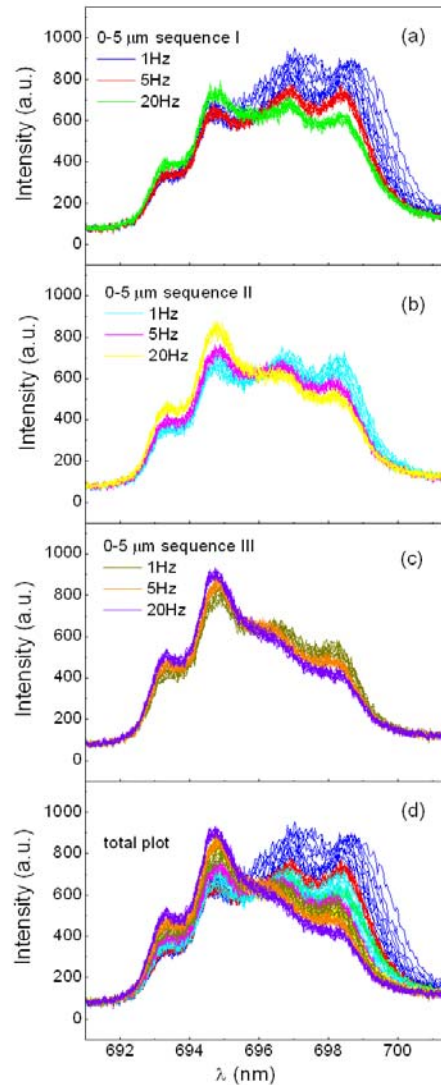


Fig. 3-42. Ruby fluorescence spectra were taken under vibration loading with piezo displacement of 5 μm . Frequency was varied in sequence of 1, 5, and 20 Hz. The sequence was repeated three times.

According to the spectral changes in Fig. 3-41, I did a set of similar experiments with designed procedures (Fig. 3-42). In the experiment, the vibration displacement was kept constant as 5 μm . I varied frequencies in sequence of 1, 5, and 20 Hz and kept the number of cycles fixed as 1200 for each frequency. At each frequency 10 spectra were taken and the exposure time for one curve was 5 s. The sequence of vibration at 1, 5 and 20 Hz was repeated for 3 times using the same sphere.

Figure 3-42(a) shows the sequence I. When vibration starts at frequency of 1

Hz, the intensity of the two peaks on the right decreases significantly. The two peaks on the left remain almost unchanged. Looking at the positions of the right peaks, there is a slight shift to the left. When the frequency is tuned to 5 Hz, the whole set of curves does not change much from the last curve taken at 1 Hz frequency. When tuning from 5 Hz to 20 Hz, however, a clear redistribution of intensity occurs. After the completion of the first sequence, the total intensity decreases apparently and this may be attributed to the formation of domains of microcracks within the optical detecting volume. The light is scattered at the boundaries of these domains and this causes the loss of intensity.

In the sequence II (Fig. 3-42b), at frequency of 1 Hz the curves again show relatively larger changes in the intensity of the two peaks on the right. These curves form a thicker band. The curves taken with 5 Hz have less change in the intensity and form a much thinner band. Until this point, slight redistribution of intensity has taken place gradually. Clearer intensity redistribution occurs when frequency changes from 5 Hz to 20 Hz. The curves under 20 Hz form a band with similar width as under 5 Hz.

The sequence III in Fig 3-42(c) mainly reproduces features similar to those of sequence II. However, one also notices that the peaks on the right become less distinguishable for the last set of curves under 20 Hz. A possible interpretation for this is that numerous states of stress exist after so many loading cycles so that the shape of the curves is smeared out.

Looking at the total plot in Fig. 3-42(d), the trend in the intensity change is explicit. The total intensity decreases but the speed of decreasing slows down with time. The two peaks on the right sink and the two peaks on the left rise. This is likely due to repopulation of domains of higher elasticity and of lower elasticity within the optical detecting volume. There are some interesting phenomena. A broader band is always formed by curves under 1 Hz frequency compared with that formed by curves under 5 or 20 Hz. The curves in cyan (1 Hz, sequence II) are supposed to be lower than the curves in green (20 Hz, sequence I) if continuous damage is expected, however, are even higher. The same case occurs to the curves in brown (1 Hz,

sequence III) and the curves in yellow (20 Hz, sequence II). According to the above observation, it seems that vibration loading at lower frequency causes more instable states of stress.

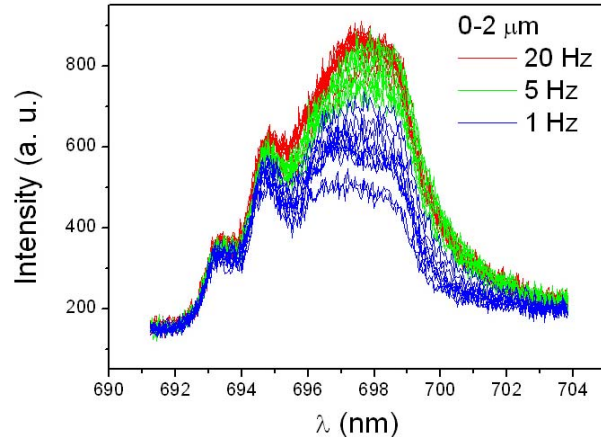


Fig. 3-43. Ruby fluorescence spectra were taken with vibration loading with piezo displacement 2 μm . Frequency was varied in sequence of 20, 5, and 1 Hz.

To verify the effect of frequency observed in Fig. 3-42, I varied the frequency in sequence of 20, 5, 1 Hz in the following experiment. All the other parameters were kept except the displacement of vibration was reduced to 2 μm . Only one sequence was done.

The total intensity of the spectra decreases apparently (Fig. 3-43). When the frequency was 20 Hz, the curves (red) do not show much change in intensity. When the frequency is tuned to 5 Hz, however, more decrease of intensity occurs, forming a thicker band. Most significant decrease of intensity takes place when the frequency is tuned to 1 Hz. Though the sequence of vibration displacement is reversed, the lower frequency still seems to generate more instability in the intensity.

Based on the above observation, I suggest the following: On the scale of detecting volume as 10^{-18} m^3 , vibration loading of the ruby sphere leads to a continuous damage above a certain limit, by which the discontinuous response, e.g. breakage, may follow. The history of the continuous damage is mainly related to the number of cycles applied. Only above non-elastic threshold, the breakage under vibration loading occurs.

During vibration loading, the total intensity decreases due to formation of smaller domains that scatter the light. The redistribution of the intensity shifting from the higher stress range (longer wavelengths) to lower stress range (shorter wavelengths) is a sign of repopulation of the domains with different elasticity within the optical detecting volume.

With the same number of loading cycles and constant displacement, vibration loading at lower frequency causes more fluctuation in the intensity (mainly decrease of the intensity), indicating less stable states of stress. Vibration loading at higher frequency causes much less fluctuation of the intensity.

4. Summary and conclusion

I studied the stresses inside the crystalline ruby microsphere ($\alpha\text{-Al}_2\text{O}_3\text{:Cr}^{3+}$, 150 μm in diameter) under uniaxial compression applied by sapphire plates ($\alpha\text{-Al}_2\text{O}_3$, 0.5mm thick). Ruby fluorescence spectra showed stress induced frequency shifts and were used as the sensor for internal stresses. By laser scanning confocal microscopy I recorded fluorescence spectra at a spatial resolution of $\sim 1\times 10^{-18} \text{ m}^3$. In this way, for the first time the stress distribution in a microcontact between a sphere and a plate of a brittle material could be measured directly.

Two-photon excitation was realized by substituting the He-Ne laser for a Ti:Sapphire pulse laser. The background intensity in fluorescence spectra was greatly reduced and the effect of multi-scattering was largely diminished. Two-photon excitation made the measurement at either very low or very high stress more accurate and further enhanced the spatial resolution, especially in axial direction, thus increased the detection depth.

Under static external loading forces, the stress distribution within a microsized spherical body of hard material (ruby crystal) was measured directly for the first time and compared to Hertz's law. The measurement was in good agreement with theoretical prediction as well as the FEM simulations. The stress across the contact area showed a hemispherical profile. The measured contact radius was in accord with the value calculated by Hertz's equation. The stresses measured along the loading axis showed a deviation from the simulation results less than 10%.

By stepwise increasing of load, stress-vs-load curves were obtained and used to analyze the stress development. From zero load to about 2 N (max. vertical stress

of 12 GPa), the deviation between the measured stress curve and the theoretical calculation was small, indicating a general elastic response of the material. Between 2 and 4 N (max. vertical stress of 12-14 GPa), the deviation between the measured curve and the calculation became larger. This was a sign of entering into non-elastic regime, within which microcracks started to form. There was a spike like decrease of stress starting at a load of 4.3-4.7 N. This was a sign of the coalescence of microcracks, which lead to a release of stress. No further rise of stress was observed thereafter. Final failure of the sphere normally occurred at about 6-7 N (max. vertical stress of 14-15 GPa). In the vicinity of the contact area fluorescence spectra with multiple distinct peaks were observed. This indicated the presence of regions of different stress, which are mechanically decoupled. Since the critical value for the yielding vertical stress of ruby is smaller than 16-20 GPa in literature, my experiment is at the verge between elastic and non-elastic regime.

Applying quasi-static loading-unloading cycles, I studied the fatigue of the brittle material at the contact region. Progressive fatigue could earliest occur when the load exceeded 1 N. As long as the load did not exceed 2 N stress-vs-load curves were normally continuous and could be described by Hertz's law with a reduced Young's modulus (increased damage). When the load exceeded 2 N, spike-like decreases of the stress could be observed. Such behavior of stress decrease was interpreted as alternatively relaxing and stressing of different micro domains sharing the total load. According to this postulation, the formation of micro-cracks on the $\sim 10 \mu\text{m}$ length scale was speculated.

A piezo driven device was used for applying vibration loading at higher frequencies with tunable vibration displacements. Two stages of response were observed under vibration loading. In the first stage continuous damage occurred and the speed of damage decreased with number of vibration cycles. The continuous damage only went on until certain limit, by which the discontinuous response, e.g. sudden breakage of the sphere, followed in the second stage. Redistributions of intensity on the fluorescence spectra were observed and I attributed this to the repopulation of micro domains of different elasticity within the optical detecting

volume.

Concerning the mechanical properties of crystalline ruby microspheres and based on the above experimental results, the following points are proposed:

- At the contact area between a ruby microsphere and a hard plate, the ruby fluorescence wavelength shift can be related to the local stresses using a proper conversion factor.
- At the microcontact of ruby, the material partly shows ductility by non-elastic response to the external loads.
- In the micro contact zone in a ruby sphere, external load causes continuous damage due to the formation and propagation of microcracks.
- Repopulation of local stress domains occurs within the regime of continuous damage, which stops at certain limit and discontinuous response, e.g. breakage, will follow.

The interaction between stress domains separated by microcracks has shown some interesting phenomena, e.g. undulating on the stress curves and intensity redistributing on the spectrum, etc. Thus for an outlook, simultaneous monitoring more than one single spot within a microcontact seems appealing. For this purpose, multi-focus optical detection or sensor group and novel design of loading methods are key elements in further studies.

Bibliography

1. Johnson, K.L., *Contact Mechanics*. 1985, Cambridge: Cambridge University Press.
2. Schönert, K., *Breakage of spheres and circular disks*. Powder Technology, 2004. **143-144**: p. 2-18.
3. Dean, W.R., I.M. Sneddon, and H.W. Parsons, *The distribution of stress in a decelerating elastic sphere*. Selected Government Research Reports, Strength and testing of materials, Part II, Testing methods and test results, 1952. **6**: p. 212.
4. Hiramatsu, Y. and Y. Oka, *Determination of the tensile strength of rock by a compression test of an irregular test piece*. Int. J. Rock Mech. Min. Sci., 1966. **3**: p. 89-99.
5. Lurje, A.J., *Räumliche Probleme der Elastizitätstheorie*. 1963, Berlin: Akademie-Verlag.
6. Shipway, P.H. and I.M. Hutchings, *Attrition of brittle spheres by fracture under compression and impact loading*. Powder Technology, 1993. **76**: p. 23-30.
7. Shipway, P.H. and I.M. Hutchings, *Fracture of brittle spheres under compression and impact loading I. Elastic stress distributions*. Philosophical Magazine A, 1993. **67(6)**: p. 1389-1404.
8. Gundepudi, M.K., et al., *Stress analysis of brittle spheres under multiaxial loading*. Powder Technology, 1997. **94**: p. 153-161.
9. Chau, K.T., et al., *Fragmentation of brittle spheres under static and dynamic compressions: experiments and analysis*. Mechanics of Materials, 2000. **32**: p. 543-554.
10. Hu, G., H. Otaki, and M. Lin, *An index of the tensile strength of brittle particles*. Mineral Engineering, 2001. **14(10)**: p. 1199-1211.

11. Tang, C.A., et al., *Numerical investigation of particle breakage as applied to mechanical crushing ---- Part I: Single-particle breakage*. International Journal of Rock Mechanics & Mining Sciences, 2001. **38**: p. 1147-1162.
12. Tang, C.A., et al., *Numerical approach to particle breakage under different loading conditions*. Powder Technology, 2004. **143-144**: p. 130-143.
13. Darvell, C.W., *Uniaxial compression tests and the validity of indirect tensile strength*. Journal of Materials Science, 1990. **25**: p. 757-780.
14. Sternberg, E. and F. Rosenthal, *The elastic sphere under concentrated loads*. Journal of Applied Mechanics, 1952. **19**: p. 413-421.
15. Hiramatsu, Y. and Y. Oka, *Determination of the tensile strength of rock by a compression test of an irregular test piece*. Int. J. Rock Mech. Min. Sci., 1966. **3**: p. 89-99.
16. Jaeger, J.C., *Failure of rocks under tensile conditions*. International Journal of Rock Mechanics and Mining Science, 1967. **4**: p. 219-227.
17. Wynnycyk, J.R., *The correlation between the strength factor and the true tensile strength of agglomerates spheres*. Canadian Journal of Chemical Engineering, 1985. **63**: p. 591-597.
18. Yoshikawa, H. and T. Sata, *Measurement of tensile strength of granular brittle materials*. Scienti@c Papers IPCR, 1960. **54(4)**: p. 389-393.
19. Bergstorm, B.H. and C.L. Sollenberger, *Kinetic energy effect in single particle crushing*. Transactions of the AIME, 1961. **220**: p. 373-379.
20. Kschinka, B.A., et al., *Strengths of glass spheres in compression*. Journal of the American Ceramic Society, 1986. **69**: p. 467-472.
21. Noyan, I.C., *Plastic-deformation of solid spheres*. Philosophical Magazine A, 1988.

- 57: p. 127-141.
22. Wong, J.Y., et al., *Strengths of green and fired spherical aluminosilicate aggregates*. Journal of the American Ceramic Society, 1987. **70**: p. 785-791.
 23. Breval, E., et al., *Microstructure, strength and environmental degradation of proppants*. Journal of Materials Science, 1987. **22**: p. 2124-2134.
 24. Santurbano, R.B., *An experimental and analytical study of the mechanics of rock particle fragmentation during impact crushing*. 1993, University of Minnesota, USA.
 25. Schoenert, K., *Breakage of spheres and circular discs*. Powder Technology, 2004. **143-144**: p. 2-18.
 26. Wu, S.Z., K.T. Chau, and T.X. Yu, *Crushing and fragmentation of brittle spheres under double impact test*. Powder Technology, 2004(143-144): p. 41-55.
 27. Salman, A.D., et al., *Descriptive classification of the impact failure modes of spherical particles*. Powder Technology, 2004(143-144): p. 19-30.
 28. Chaudhri, M.M., *Impact breakage of semi-brittle spheres*. Powder Technology, 2004. **143-144**: p. 31-40.
 29. Pitchumani, R., et al., *Measurement and characterization of particle strength using a new robotic compression tester*. Powder Technology, 2004. **143-144**: p. 563-64.
 30. PINIT, P. and E. UMEZAKI, *Full-Field Determination of Principal-Stress Directions Using Photoelasticity with Plane-Polarized RGB Lights*. OPTICAL REVIEW, 2005. **12**(3): p. 228-232.
 31. Mitchell, N.B., Materials Research and Standards, 1961. **1**: p. 780.
 32. Frocht, M.M., in *Photoelasticity*. 1948, Wiley: London.

33. Antonyuk, S., et al., *Breakage behaviour of spherical granulates by compression*. Chem. Eng. Sci., 2005. **60**: p. 4031-4044.
34. Krogh, S.R., *Crushing characteristics*. Powder Technology, 1980. **27**: p. 171-181.
35. Pauw, O.G. and M.S. Maré, *The determination of optimum impact-breakage routes for an ore*. Powder Technol., 1988. **54**: p. 3-13.
36. Vervoorn, P.M.M. and L.G. Austin, *The analysis of repeated breakage events as an equivalent rate process*. Powder Technology, 1990. **63**: p. 141-147.
37. Tavares, L.M. and R.P. King, *Modeling of particle fracture by repeated impacts using continuum damage mechanics*. Powder Technol., 2002. **123**: p. 138-146.
38. Vaughan, D.A.J. and F. Guiu, *Cyclic fatigue of advanced ceramics by repeated indentation*. Brit. Ceram. Soc., 1987. **39**: p. 101-107.
39. Reece, M. and F. Guiu, *Repeated indentation method for studying cyclic fatigue in ceramics*. J. Am. Ceram. Soc., 1990. **73**: p. 1004-1013.
40. Reece, M. and F. Guiu, *Indentation fatigue of high-purity alumina in fluid environment*. J. Am. Ceram. Soc., 1991. **74**: p. 148.
41. Takakura, E. and S. Horibe, *Fatigue damage in ceramic material caused by repeated indentations*. J. Mat. Sci., 1992. **27**: p. 6151-6158.
42. Guillou, M.-O., J.L. Henshall, and R.M. Hooper, *Indentation cyclic fatigue of single-crystal magnesium oxide*. J. Am. Ceram. Soc., 1993. **76**: p. 1832-1836.
43. Henshall, J.L., M.-O. Guillou, and R.M. Hooper, *Point contact surface fatigue in zirconia ceramics*. Tribol. Int., 1995. **17**: p. 247-253.
44. Guiberteau, F., et al., *Indentation fatigue: a simple cyclic Hertzian test for measuring damage accumulation in polycrystalline ceramics*. Phil. Mag. A, 1993. **68**: p. 1003-1016.

45. Padture, N.P. and B.R. Lawn, *Contact fatigue of a silicon carbide with a heterogeneous grain structure*. J. Am. Ceram. Soc., 1995. **78**: p. 1431-1438.
46. Padture, N.P. and B.R. Lawn, *Fatigue in ceramics with interconnecting weak interfaces: a study using cyclic Hertzian contacts*. Acta metall. mater., 1995. **43**: p. 1609-1617.
47. Kim, D.K., et al., *Cyclic fatigue of intrinsically brittle ceramics in contact with spheres*. Acta mater., 1999. **42**: p. 4711-4725.
48. Lee, S.K. and B.R. Lawn, *Contact fatigue in silicon nitride*. J. Am. Ceram. Soc., 1999. **82**: p. 1281-1288.
49. Jung, Y.-G., et al., *Lifetime-limiting strength degradation from contact fatigue in dental ceramics*. J. Dent. Res., 2000. **79**: p. 722-731.
50. Grabner, L., *Spectroscopic technique for the measurement of residual stress in sintered Al₂O₃*. J. Appl. Phys., 1978. **49**: p. 580-583.
51. Molis, S.E. and D.R. Clarke, *Measurement of stresses using fluorescence in an optical microprobe: Stresses around indentations in a chromium-doped sapphire*. J. Am. Ceram. Soc., 1990. **73**: p. 3189-3194.
52. Eremets, M.I., et al., *Deformation of material under indenter for hardness. Ruby as local pressure sensor*. High Pressure Research, 1991. **7**: p. 219-221.
53. Yang, X. and R.J. Young, Acta Metall. Mater., 1995. **43**: p. 2407-2416.
54. Zhao, F.M., et al., *Photoelastic analysis of matrix stresses around high modulus sapphire fibre by means of phase-stepping automated polariscope*. Composites: Part A, 2005. **36**: p. 229-244.
55. Hayazawa, N., et al., *Highly sensitive strain detection in strained silicon by surface-enhanced Raman spectroscopy*. Appl. Phys. Lett., 2005. **86**: p. 263114.

56. Cronin, S.B., et al., *Resonant Raman spectroscopy of individual metallic semiconducting single-wall carbon nanotubes under uniaxial strain*. Phys. Rev. B, 2005. **72**: p. 035425.
57. Jiang, C., H. Ko, and V.V. Tsukruk, *Strain-sensitive Raman modes of carbon nanotubes in deflecting freely suspended nanomenbranes*. Adv. Mater., 2005. **17**: p. 2127-2131.
58. Wang, X.B., et al., *Near infrared excited micro-Raman spectra of 4:1 methanol-ethanol mixture and ruby fluorescence at high pressure*. J. Appl. Phys., 1999. **85**: p. 8011-8017.
59. Demtroder, W., *Laser Spectroscopy - Basic Concepts and Instrumentation*. 1982, Springer: Berlin. p. 436-443.
60. Holzapfel, W.B. and N.S. Isaacs, eds. *High-Pressure Techniques in Chemistry and Physics: A Practical Approach*. 1997.
61. Barnett, J.D., S. Block, and G.J. Piermarini, *Optical Fluorescence System for Quantitative Pressure Measurement in Diamond-Anvil Cell*. Review of Scientific Instruments, 1973. **44**(1): p. 1-9.
62. Piermarini, G.J. and S. Block, *Ultrahigh Pressure Diamond-Anvil Cell and Several Semiconductor Phase-Transition Pressures in Relation to Fixed-Point Pressure Scale*. Review of Scientific Instruments, 1975. **46**(8): p. 973-979.
63. Hirschfeld, T., et al., *Fiber optics temperature and pressure probe*, in *Analytical Spectroscopy: Analytical Chemistry Symposia Series*, W.S. Lyon, Editor. 1984, Elsevier Science Publishers B.V.: Amsterdam. p. 19-23.
64. Adams, D.M., R. Appleby, and S.K. Sharma, *Spectroscopy at very high-pressures. X. Use of ruby R-lines in estimation of pressure at ambient and at low-temperatures*. Journal of Physics E-Scientific Instruments, 1976. **9**(12): p. 1140-1144.

65. Hirsch, K.R. and W.B. Holzapfel, *A realtime ruby luminescence spectrometer for pressure determinations*. Journal of Physics E-Scientific Instruments, 1983. **16**(5): p. 412-417.
66. Eggert, J.H., K.A. Goettel, and I.F. Silvera, *Ruby at high pressure. I. Optical line shifts to 156 GPa*. Physical Review B, 1989. **40**: p. 5724-5732.
67. He, J. and D.R. Clarke, *Determination of the piezospectroscopic coefficients for chromium-doped sapphire*. J. Am. Ceram. Soc., 1995. **78**: p. 1347-1353.
68. Ma, Q. and D.R. Clarke, *Stress measurement in single-crystal and polycrystalline ceramics using their optical fluorescence*. J. Am. Ceram. Soc., 1993. **76**: p. 1433-1440.
69. Ma, Q. and D.R. Clarke, *Measurement of residual stress in sapphire fibre composites using optical fluorescence*. Acta metall. mater., 1993. **41**: p. 1817-1823.
70. Ma, Q., et al., *Mechanics of the push-out process in situ measurement of the stress distribution along embedded sapphire fibres*. Acta metall. mater., 1994. **42**: p. 3299-3308.
71. Ma, Q., et al., *Residual stress in Al₂O₃-ZrO₂ composites: A test of stochastic stress models*. Acta metall. mater., 1994. **42**: p. 1673-1681.
72. Rhee, Y.W., et al., *Brittle fracture versus quasi plasticity in ceramics: A simple predictive index*. J. Am. Ceram. Soc., 2001. **84**: p. 561-565.
73. Boyde, A., *Bibliography on confocal microscopy and its applications*. Scanning, 1994. **16**: p. 33-56.
74. Pawley, J.B., *Handbook of Biological Confocal Microscopy*. 2nd ed. 1995, New York, London: Plenum Press.
75. Lopez-Cepero, J.M., et al., *Fractographic studies of sapphire fibers using laser*

- scanning confocal microscope*. Key Engineering Materials, 2005. **290**: p. 280-283.
76. Göppert-Mayer, M., Ann. Phys., 1931. **9**: p. 273-294.
 77. Denk, W., J. Strickler, and W. Webb, *Two-photon laser scanning fluorescence microscopy*. Science, 1990. **248**(4951): p. 73-6.
 78. Schawlow, A.L., *Fine structure and properties of chromium fluorescence in aluminum and magnesium oxide*, in *Advances in Quantum Electronics*, J.R. Singer, Editor. 1961, Columbia University Press: New York. p. 50-64.
 79. Feher, E. and M.D. Sturge, *Effect of stress on the trigonal splittings of d3 ions in sapphire ($\alpha\text{-Al}_2\text{O}_3$)*. Phys. Rev., 1968. **172**: p. 244-249.
 80. Kaplyanskii, A.A. and A.K. Przhevuskii, Dokl. Akad. Nauk SSSR, 1962. **142**: p. 313.
 81. Chen, Y., et al., *Pressure distribution in a mechanical microcontact*. Appl. Phys. Lett., 2006. **88**: p. 234101.
 82. Huber, M.T., *Zur Theorie der Berührung fester elastischer Körper*. Annalen der Physik, 1904. **14**: p. 153-163.
 83. Maugis, D., *Contact, Adhesion and Rupture of Elastic Solids*. Solid-State Sciences, ed. M. Cardona, et al. Vol. 130. 2000, Berlin: Springer.
 84. Hertz, H., *Über die Berührung fester elastischer Körper*. J. Reine Angewandte Mathematik, 1882. **92**: p. 156-171.
 85. Mashimo, T., Y. Hanaoka, and K. Nagayama, *Elastoplastic properties under shock compression of Al_2O_3 single crystal and polycrystal*. J. Appl. Phys., 1987. **63**: p. 327-336.
 86. Kachanov, L.M., *Time of the rupture process under creep conditions*. Izv. Acad. Nauk S.S.S.R., Otd. Tekh. Nauk., 1958. **8**: p. 26-31.

87. Loland, K.E., *Continuous damage model for load-response estimation of concrete*. Cem. Concr. Res., 1980. **10**: p. 395-402.
88. Taylor, L.M., E.P. Chen, and J.S. Kuszmaul, *Microcrack-induced damage accumulation in brittle rock under dynamic loading*. Comput. Methods Appl. Mech. Eng., 1986. **55**: p. 301-320.
89. Chen, Y., et al., *Stress and failure at mechanical contacts of microspheres under uniaxial loading*. J. Appl. Phys., 2007. **101**(8): p. 084908.
90. Page, T.F., W.C. Oliver, and J.C. McCallum, *The deformation behavior of ceramic crystals subjected to very low load (nano) indentation*. J. Mater. Res., 1992. **7**: p. 450.
91. Nowak, R. and M. Sakai, *The anisotropy of surface deformation of sapphire: Continuous indentation of triangular indenter*. Acta metall. mater., 1994. **42**: p. 2879-2891.
92. Nowak, R., T. Sekino, and K. Niihara, *Non-linear surface deformation of the (1010) plane of sapphire: Identification of the linear features around spherical impressions*. Acta mater., 1999. **47**: p. 4329-4338.

Curriculum Vitae

First name: Yun
Last name: Chen
Date of birth: 11. Oct. 1980
Place of birth: Wuxi, China
Address: Ackermannweg 10, D-55128 Mainz, Germany
Mobile: +49 (0) 176 2401 0128
Tel: +49 (0) 6131 8374 090
E-mail: chen@mpip-mainz.mpg.de

Education:

- PhD Oct. 2005-Sep. 2007: Max Planck Institute for Polymer Research and University of Siegen, Germany
- Master Oct. 2003-Sep. 2005: University of Siegen, Germany
- Bachelor Sep. 1999-Jun. 2003: Shanghai JiaoTong University, Shanghai, China
- High school Sep. 1993-Jun. 1999: Wuxi, China
- Primary school Sep. 1987-Jun. 1993: Wuxi, China

Publications:

- **Yun Chen**, Kaloian Koynov, and Hans- Jürgen Butt, Contact fatigue in an alumina microcontact: A confocal laser scanning microscope study. *Journal of Materials Research*, 2007 (in press for Nov. issue)
- H.-J. Butt, R. Berger, E. Bonaccorso, **Y. Chen**, J. Wang. Impact of atomic force microscopy on interface and colloid science. *Advances in Colloid Interface and Science* 133, p. 91, 2007
- **Yun Chen**, Andreas Best, Thomas Haschke, *et al.*, Stress and failure at mechanical contacts of microspheres under uniaxial loading. *Journal of Applied Physics* (101) 084908, 2007
- **Yun Chen**, Andreas Best, Hans-Jürgen Butt, *et al.*, Pressure distribution in a mechanical microcontact. *Applied Physics Letters* 88 (23) 234101, 2006